



**NTNU – Trondheim**  
Norwegian University of  
Science and Technology

# Transient LDV-measurements in the draft tube of a high head Francis turbine

**Carl Werdelin Bergan**

Master of Science in Mechanical Engineering

Submission date: June 2014

Supervisor: Ole Gunnar Dahlhaug, EPT

Norwegian University of Science and Technology  
Department of Energy and Process Engineering



EPT-M-2014-12

**MASTER THESIS**

For

Carl Bergan

Spring 2014

**Transient LDV-measurements in the draft tube of a high head Francis turbine***Transient LDV-målinger i sugerøret til en høytrykks Francis turbin***Background**

Francis-99 is a set of upcoming workshops jointly organized by the Norwegian University of Science and Technology (NTNU), Norway and Luleå University of Technology (LTU), Sweden in the same spirit as the previous Turbine-99 workshops. The Francis-99 workshops aim during the coming years to determine the state of the art of high head Francis turbine simulations under steady and transient operating conditions as well as promote their development and knowledge dissemination openly.

A high head Francis turbine model, named the Tokke model, has been designed and experimentally investigated in the Waterpower Laboratory at NTNU. The complete geometry of the model and mesh are now freely available on the present site. NTNU and LTU expect this geometry to become with time a reference test case to the hydraulic community for research and development and the workshops a meeting place to discuss developments, potentials, issue on a common and open test case.

The student will carry out LDV-measurements on the existing turbine geometry, in order to investigate the transient flow characteristics in the draft tube. Another student will carry out CFD-analysis in the draft tube and they will work together on both CFD-analysis and LDV-measurements.

**Objective**

Carry out non-stationary LDV-measurements of the flow in the draft tube of a high head Francis turbine and compare with CFD-analysis.

**The following tasks are to be considered:**

1. Literature survey
  - a. Transient LDV-measurements in swirling flows
2. Software knowledge
  - a. Get familiar with the Dantec software to analyse the LDV-measurements
  - b. Get familiar with the Dantec software to operate the position system
3. Preparation of the test rig
  - a. Modifications of the draft tube cone
  - b. Set up the position system and LDV in the draft tube cone
4. Measurements
  - a. Performance of the model turbine
  - b. LDV-measurements in the draft tube
  - c. Pressure pulsations in the draft tube and upstream the runner (if there is time available)
5. CFD-analysis (this will be carried out together with another student)
  - a. Transient CFD-analysis of the runner and prototype

b. Comparison of the LDV-measurements and CFD-analysis

-- ” --

Within 14 days of receiving the written text on the master thesis, the candidate shall submit a research plan for his project to the department.

When the thesis is evaluated, emphasis is put on processing of the results, and that they are presented in tabular and/or graphic form in a clear manner, and that they are analyzed carefully.

The thesis should be formulated as a research report with summary both in English and Norwegian, conclusion, literature references, table of contents etc. During the preparation of the text, the candidate should make an effort to produce a well-structured and easily readable report. In order to ease the evaluation of the thesis, it is important that the cross-references are correct. In the making of the report, strong emphasis should be placed on both a thorough discussion of the results and an orderly presentation.

The candidate is requested to initiate and keep close contact with his/her academic supervisor(s) throughout the working period. The candidate must follow the rules and regulations of NTNU as well as passive directions given by the Department of Energy and Process Engineering.

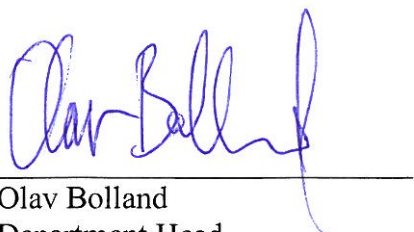
Risk assessment of the candidate's work shall be carried out according to the department's procedures. The risk assessment must be documented and included as part of the final report. Events related to the candidate's work adversely affecting the health, safety or security, must be documented and included as part of the final report. If the documentation on risk assessment represents a large number of pages, the full version is to be submitted electronically to the supervisor and an excerpt is included in the report.

Pursuant to “Regulations concerning the supplementary provisions to the technology study program/Master of Science” at NTNU §20, the Department reserves the permission to utilize all the results and data for teaching and research purposes as well as in future publications.

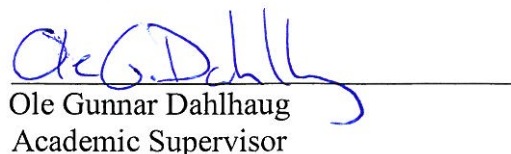
The final report is to be submitted digitally in DAIM. An executive summary of the thesis including title, student's name, supervisor's name, year, department name, and NTNU's logo and name, shall be submitted to the department as a separate pdf file. Based on an agreement with the supervisor, the final report and other material and documents may be given to the supervisor in digital format.

- Work to be done in the Waterpower laboratory  
 Field work

Department of Energy and Process Engineering, 14. January 2014



Olav Bolland  
Department Head



Ole Gunnar Dahlhaug  
Academic Supervisor

Research Advisor: Michel Cervantes, Professor

Luleå University of Technology

NORWEGIAN UNIVERSITY OF SCIENCE AND TECHNOLOGY

## *Abstract*

Department of Energy and Process Engineering

### **Transient LDA Measurements in the Draft Tube of a High Head Francis Turbine**

by Carl Bergan

Francis-99 is a series of upcoming workshops aimed at determining the state of the art of high head Francis turbine simulations. The scope of this essay is to provide empirical data to serve as validation for the CFD simulations.

Axial and tangential velocity profiles were measured for a model of the Tokke runner while operating in part load, best efficiency, and full load, at two different locations in the draft tube cone: 64 mm and 382 mm below the draft tube inlet. The results were phase resolved in order to calculate normal Reynolds stresses at the different operating conditions, and the results have been compared with computer simulations. The resulting velocity profiles have been evaluated with respect to the governing equations, and the correlation between velocity profiles, pressure gradients and normal stresses has been discussed. The effect of head on the velocity profiles has been evaluated, and found to have only a small impact on the reduced velocity profiles, both axially and tangentially. The repeatability of the test rig was also tested, and found to be within acceptable limits.

The reliability of the measured velocity profiles is considered high enough to be admissible as validation data for the Francis-99 workshop.

The simulated results show good agreement with the measured velocity profiles for axial flow, but show great discrepancies for the tangential velocity profiles. However, some similarities can be seen between the simulated and measured results, and further work is required in this area.



# Sammendrag

Aksiale og tangensielle hastighetsprofiler har blitt målt for modellløpehjulet Tokke under dellast, bestpunkt, og fullast. Målingene ble gjennomført på to forskjellige steder i sugerørskonusen: 64 mm og 382 mm under løpehjulets utløp. Resultatene har blitt faseanalysert, og normalspenninger i væsken har blitt beregnet på bakgrunn av dette. Måleresultatene har blitt sammenlignet med CFD-simuleringer av løpehjulet under de aktuelle driftspunktene. De målte hastighetsprofilene har blitt diskutert med utgangspunkt i Euler-ligningen, og korrelasjonen mellom hastighetsprofiler, trykkgradienter og normalspenninger har blitt diskutert. Etter prøvemålinger viser det seg at trykket har liten påvirkning på de reduserte hastighetsprofiler, både i aksiell og tangensiell retning. Testtriggens repeterbarhet har også blitt vurdert, og konkludert med å være innenfor akseptable grenser. Påliteligheten av de målte hastighetsprofilene anses høy nok til å kunne brukes som valideringsdata for Francis-99 workshopen. De simulerte resultater viser god overensstemmelse med den målte hastighetsprofilene for aksiellhastigheten, men viser store avvik for de tangensiellhastigheten. Noen formligheter kan sees i hastighetsprofilene, ytterligere arbeid er nødvendig på dette området.

# *Acknowledgements*

I would like to thank Ole Gunnar Dahlhaug for his valuable guidance in the process, as I am quite sure that this thesis could not have been written without his help.

I would also like to thank Joel Sundström and Kaveh Amiri for our cooperation in the LDA measurements; working together in the lab has been educational as well as enjoyable. I would also like to thank Kaveh in particular for sharing his expertise in measuring techniques with me, and Joel for a substantial amount of help with the post processing of the results. In addition, I would like to thank Michel Cervantes for his contribution whenever we encountered problems in our measurements. I would also like to thank the other students at the Waterpower Laboratory. They have made my time here an enjoyable one, and I have learned a lot from discussing problems in my thesis with them. I would like to thank the technicians at the Waterpower Laboratory for their continued assistance with the practical part of my thesis, and I would like to extend my gratitude to Joar Grilstad in particular for his invested time in helping us overcome our issues with data acquisition. I would also like to thank James Dawson and Per Åge Krogstad for their assistance in setting up, adjusting, and using the LDA system. Their knowledge in this field was invaluable.

Finally I would like to thank my parents, Lise Bergan and Jesper Simonsen, for their personal support in my academic progression and in my research.



# Contents

<b>Objective</b>	<b>i</b>
<b>Abstract</b>	<b>iii</b>
<b>Sammendrag</b>	<b>iii</b>
<b>Acknowledgements</b>	<b>vi</b>
<b>Contents</b>	<b>vii</b>
<b>List of Figures</b>	<b>ix</b>
<b>List of Tables</b>	<b>xi</b>
<b>Abbreviations</b>	<b>xiii</b>
<b>Nomenclature</b>	<b>xv</b>
<b>1 Introduction</b>	<b>1</b>
1.1 Background . . . . .	1
1.1.1 Francis-99 . . . . .	2
1.1.2 Previous work . . . . .	2
<b>2 Theory of the flow</b>	<b>5</b>
2.1 Theory of turbulence . . . . .	5
2.2 Rankine Vortex . . . . .	6
2.3 The Euler equations for swirling flows . . . . .	7
2.4 Boundary Layers . . . . .	8
2.5 Flow separation . . . . .	9
<b>3 Lab Preparation</b>	<b>11</b>
3.1 HSE: lab safety . . . . .	11
3.2 Experimental Setup . . . . .	11
3.2.1 Measuring positions . . . . .	13
3.2.2 Compensations due to weak laser . . . . .	13

3.2.3	Shaft encoder . . . . .	14
3.2.4	Optical alignment . . . . .	15
3.3	Experimental Method . . . . .	16
3.4	Operating Conditions . . . . .	17
<b>4</b>	<b>Data analysis</b>	<b>19</b>
4.1	Waveform coupling . . . . .	19
4.1.1	Logging rate . . . . .	20
4.1.2	Cross correlation . . . . .	20
4.2	Phase resolving . . . . .	21
<b>5</b>	<b>Results</b>	<b>23</b>
5.1	Velocity profiles . . . . .	23
5.2	Phase-averaged velocity . . . . .	25
5.3	Turbulence . . . . .	25
5.4	CFD velocity profile comparison . . . . .	26
<b>6</b>	<b>Discussion</b>	<b>29</b>
6.1	Evaluation of the experimental setup . . . . .	29
6.1.1	Repeatability of the Francis rig . . . . .	29
6.1.2	Sources of errors . . . . .	30
6.2	Choice of operating point . . . . .	34
6.3	Flow properties . . . . .	34
6.3.1	Flow profile similarities . . . . .	35
6.3.2	Back flow: The dead core . . . . .	36
6.3.3	The Rankine Vortex . . . . .	38
6.3.4	Blade wakes . . . . .	39
6.3.5	Turbulence . . . . .	40
6.4	CFD results . . . . .	41
<b>7</b>	<b>Conclusions</b>	<b>43</b>
7.1	Conclusions . . . . .	43
7.2	Further Work . . . . .	44
	<b>References</b>	<b>45</b>
<b>A</b>	<b>Laser Data Sheet</b>	<b>I</b>
<b>B</b>	<b>Calibration Documents</b>	<b>V</b>
<b>C</b>	<b>Phase-resolved results</b>	<b>XVII</b>

# List of Figures

2.1	Example of triple decomposition of velocity measurements . . . . .	6
2.2	The Rankine Vortex . . . . .	7
2.3	Example of a Flat-plate boundary layer . . . . .	8
2.4	Pressure-driven flow separation . . . . .	9
2.5	Reduced divergence in draft tube due to flow separation . . . . .	10
3.1	Sketch of the closed loop test rig . . . . .	12
3.2	Measuring sections in the draft tube cone . . . . .	13
3.3	Finding the wall . . . . .	16
5.1	Reduced velocity profiles for part load . . . . .	24
5.2	Reduced velocity profiles for BEP . . . . .	24
5.3	Reduced velocity profiles for full load . . . . .	24
5.4	Phase averaged velocity for BEP, position I . . . . .	25
5.5	Phase averaged velocity for BEP, position II . . . . .	25
5.6	Reynolds normal stresses for part load . . . . .	26
5.7	Reynolds normal stresses for BEP . . . . .	26
5.8	Reynolds normal stresses for full load . . . . .	27
5.9	Reduced velocity profiles for BEP at section I produced with CFD compared with LDA results . . . . .	27
5.10	Reduced velocity profiles for BEP at section II produced with CFD compared with LDA results . . . . .	27
6.1	Locating the draft tube wall . . . . .	31
6.2	Sensitivity analysis . . . . .	34
6.3	Direction of decreasing pressure in the draft tube . . . . .	37
6.4	Swirl Numbers . . . . .	37
6.5	Axial velocity for swirling flow . . . . .	38
6.6	Contours of phase resolved tangential velocity at BEP, position I . . . . .	40
C.1	Phase resolved velocity for part load, position I . . . . .	XVII
C.2	Phase resolved velocity for part load, position II . . . . .	XVII
C.3	Phase resolved velocity for BEP, position I . . . . .	XVIII
C.4	Phase resolved velocity for BEP, position II . . . . .	XVIII
C.5	Phase resolved velocity for full load, position I . . . . .	XIX
C.6	Phase resolved velocity for full load, position II . . . . .	XIX



# List of Tables

3.1	Francis-99 operating conditions . . . . .	17
3.2	Operating conditions used in this thesis . . . . .	17
5.1	$U_{BULK}$ for the different operating points . . . . .	23
6.1	Repeatability of the Francis rig . . . . .	30
6.2	Axial pressure gradients in the draft tube cone . . . . .	36



# Abbreviations

<b>BEP</b>	<b>B</b> est <b>E</b> fficiency <b>P</b> oint
<b>BSA</b>	<b>B</b> urst <b>S</b> pectrum <b>A</b> nalyzer
<b>CFD</b>	<b>C</b> omputational <b>F</b> luid <b>D</b> ynamics
<b>DAQ</b>	<b>D</b> ata <b>A</b> cquisition
<b>HSE</b>	<b>H</b> ealth, <b>S</b> afety, and <b>E</b> nvironment
<b>LDA</b>	<b>L</b> aser <b>D</b> oppler <b>A</b> nomometry
<b>LDV</b>	<b>L</b> aser <b>D</b> oppler <b>V</b> elocimetry
<b>NI</b>	<b>N</b> ational <b>I</b> nstruments
<b>NTNU</b>	<b>N</b> orges <b>T</b> eknisk- <b>N</b> aturvitenskapelige <b>U</b> niversitet (The Norwegian University of Science and Technology)
<b>PIV</b>	<b>P</b> article <b>I</b> mage <b>V</b> elocimetry
<b>RPM</b>	<b>R</b> otations <b>P</b> er <b>M</b> inute
<b>RVR</b>	<b>R</b> otating <b>V</b> ortex <b>R</b> ope
<b>USB</b>	<b>U</b> niversal <b>S</b> erial <b>B</b> us





# Nomenclature

## Roman symbols

$D$	Runner diameter	[m]
$f_M$	Master timebase frequency	[MHz]
$F_s$	Sampling rate	[Hz]
$g$	Gravitational acceleration	[m/s <sup>2</sup> ]
$H$	Head	[m]
$k$	Turbulence model constant	[-]
$m$	Sampling rate constant	[-]
$n$	Runner frequency	[Hz]
$n_{ED}$	Dimensionless rotational speed	[-]
$N_s$	Number of samples	[-]
$p$	Pressure	[Pa]
$Q$	Flow rate	[m <sup>3</sup> /s]
$Q_{ED}$	Dimensionless flow rate	[-]
$r^*$	Normalized radius	[-]
$r$	Radial coordinate	[m]
$R$	Pipe radius	[m]
$R_S$	Solid-body-rotation radius	[m]
$S$	Swirl Number	[-]
$u$	Velocity	[m/s]
$\bar{u}$	Time-averaged velocity	[m/s]
$\tilde{u}$	Phase-dependent velocity variations	[m/s]
$\langle u(x, t) \rangle$	Phase resolved velocity	[m/s]

---

$u^*$	Reduced axial velocity	[-]
$U_{BULK}$	Bulk velocity	[m/s]
$u'$	Velocity fluctuation	[m/s]
$u'^2$	Normal Reynolds stress (axial)	[-]
$v^*$	Reduced tangential velocity	[-]
$v'^2$	Normal Reynolds stress (tangential)	[-]

**Greek symbols**

$\epsilon$	Turbulence model constant	[-]
$\eta$	Efficiency	[%]
$\rho$	Density	[kg/m <sup>3</sup> ]
$\tau$	Time lag	[s]
$\omega$	Turbulence model constant	[-]

**Common subscripts**

$r$	Radial direction
$\theta$	Rotational direction
$z$	Axial direction

# 1 | Introduction

## 1.1 Background

The increased use of hydro power in supplying peak-demand power in conjunction with nuclear fission, coal, and other steady, slowly regulated power sources causes an increase in part load operation on hydro power plants [1]. It is a well known fact that running a turbine outside of its design point can cause a lot of problems, such as pressure pulsations, power swings, and reduced lifetime, among other things. Part of the challenge arises in the draft tube cone, a turbine component dominated by complicated flow fields, high pressure gradients, high Reynolds stresses, and low-frequency high amplitude pressure pulsations [1].

The purpose of this thesis is to investigate the flow field in the draft tube of the model of the Tokke runner at the Waterpower Laboratory at the Norwegian University of Science and Technology (NTNU), with focus on velocity profiles, and turbulence properties, in order to serve as validation data for Computational Fluid Dynamics (CFD). The measurements will be performed with 2D Laser Doppler Anemometry (LDA), for a high head Francis runner operating at part load, the Best Efficiency Point (BEP), and full load. The experimental results will be compared with simulation results from the master thesis of Ruben Moritz of NTNU, 2014.

### 1.1.1 Francis-99

Francis 99 is a series of workshops in which several aspects of Francis turbine operation will be investigated. The scope of this thesis is LDA measurements of the draft tube flow for the Tokke model runner at three given operating points, in order to obtain velocity profiles, turbulence, phase-averaged velocities and, if possible, other transient phenomena.

The results from this thesis will serve as validation for the numerical simulation of the same phenomena, in order to determine the state of the art of numerical simulation of transient phenomena in draft tube flow.

### 1.1.2 Previous work

Both swirling flow and Francis operating conditions have been extensively investigated. The effect of different semi-tapered cones attached to the runner on the velocity field has been investigated by Veveke [2]. The experiments were performed using Laser Doppler Velocimetry (LDV) on a model Francis turbine at the Waterpower Laboratory at NTNU, and video recording was done in order to visualize the Rotating Vortex Rope (RVR) behavior.

Dahlhaug [3] used LDA to investigate the velocities in a pure swirling flow where the swirl is artificially induced, in addition to conventional model draft tube measurements.

LDA measurements have been performed on a model Kaplan turbine by Kaveh [4], modeling the Projus U9 runner. This investigation focused on the velocity in the blade channels and the runner outlet, while simultaneously measuring the pressure distribution in the draft tube cone.

Glas, Forstner, Kuhn, and Jaberg [5] did extensive work in LDV data analysis regarding periodic phenomena in the flow. This theory is applicable in many cases

when LDV is utilized, providing a tool for obtaining valuable phase-resolved data and components of the Reynolds stress tensor.

Trivedi, Cervantes, Gandhi, and Dahlhaug [6] have performed extensive pressure measurements on the Tokke model runner in conjunction with the Francis-99 workshop, as well as turbine performance measurements. Pressure-time measurements were performed over several operating points, numerical simulation was performed using two turbulent models, shear stress transport  $k - \omega$  and standard  $k - \epsilon$ .

The flow in a Francis turbine spiral casing has been investigated with LDV by Antonesen [7].

Swirling flow in a conical diffuser has been investigated by Senoo, Kawaguchi, and Nagata [8], in which the diffuser demonstrates a higher pressure recovery coefficient with a diffuser angle of 8 degrees and moderate swirl. Pressure and velocity has been measured for swirling non-cavitating flows by Guarga, Gracia, Sánchez, and Rodal [9], in which the size of the rotational core displays a dependency on the angular momentum in the flow. Velocity and pressure fluctuations in a Francis draft tube has been investigated by Mollenkopf and Raabe [10] using piezo-electric pressure transducers and hot-film anemometry.



## 2 | Theory of the flow

### 2.1 Theory of turbulence

Turbulence is a flow regime characterized by three dimensional fluctuations, random variations, self-sustaining motion, strong mixing, and tightly packed eddies. Turbulence is a complex phenomena that will never be possible to analytically quantify completely, due to its chaotic nature. Many books and papers have been published in the field of turbulence, with hundreds of papers being published every year on the subject [11]. Turbulence will not be discussed in-depth in this thesis, but simple velocity decomposition will be explained.

The generally accepted method of dealing with turbulence in velocity measurements is to decompose the individual velocity components.

A typical velocity measurement will not show the constant mean velocity in the flow, but rather a flow with seemingly random fluctuations about a mean. Subtracting the mean velocity, only this seemingly random fluctuation is left.

Depending on the flow, there may be some periodic phenomena, (axle rotation, blade wakes, vortex shedding etc.) which will show up in these seemingly random velocity fluctuations. Resolving for the periodic velocity fluctuations, the velocity can be decomposed as shown in Equation 5.2. This method is known as Reynolds triple decomposition [4]. An example of such decomposition is shown in Fig. 2.1. In this example, the measurements have been resolved according to runner phase.

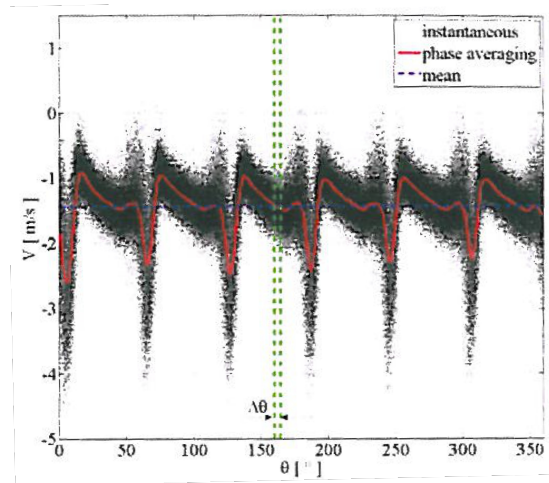


FIGURE 2.1: Example of triple decomposition of velocity measurements. This example is taken from velocity measurements in a Kaplan draft tube [4].

## 2.2 Rankine Vortex

For rotating flows in a pipe, the tangential velocity profile often takes on the form of a Rankine Vortex, a combination of a solid-body rotation and a free vortex [3]. This type of velocity profile is illustrated in Fig. 2.2.

In rotating pipe flows, a commonly used parameter for characterizing the flow is the *Swirl number*, or *Swirl intensity*, which is defined as the ratio between the tangential and axial momentum [3].

$$S = \frac{\int_0^R r^2 \cdot \rho \cdot u_z \cdot u_\theta \cdot dr}{R \cdot \int_0^R r \cdot \rho \cdot u_z^2 \cdot dr} \quad (2.1)$$

From Equation 2.1, it is clear that a larger relative rotation in the draft tube will yield a larger swirl number.



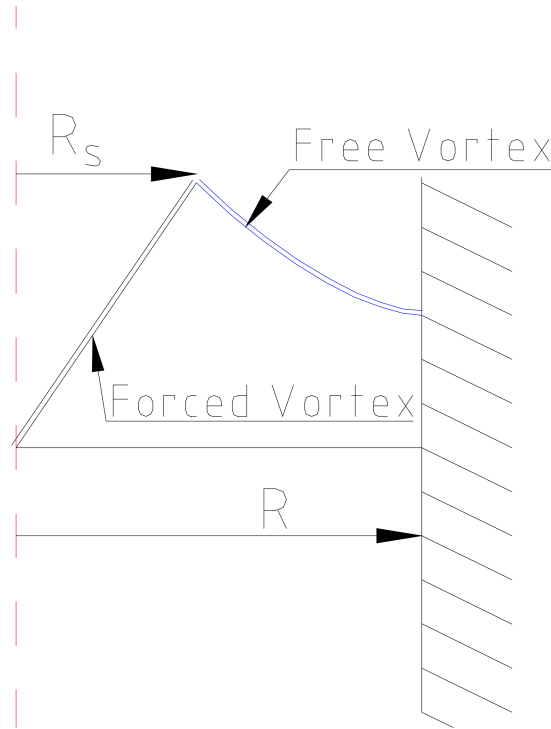


FIGURE 2.2: The Rankine Vortex. This flow regime is composed of a solid body rotation and a free vortex [12].

## 2.3 The Euler equations for swirling flows

Simplifying the Navier-Stokes equation by removing viscous terms, we are left with the Euler equations, given in Equation 2.2, obtained from [11].

$$\frac{\partial u_r}{\partial t} + u_r \cdot \frac{\partial u_r}{\partial r} + \frac{u_\theta}{r} \cdot \frac{\partial u_r}{\partial \theta} - \frac{u_\theta^2}{r} + u_z \cdot \frac{\partial u_r}{\partial z} = g_r - \frac{1}{\rho} \cdot \frac{\partial p}{\partial r}$$

$$\frac{\partial u_\theta}{\partial t} + u_r \cdot \frac{\partial u_\theta}{\partial r} + \frac{u_\theta}{r} \cdot \frac{\partial u_\theta}{\partial \theta} - \frac{u_r \cdot u_\theta}{r} + u_z \cdot \frac{\partial u_\theta}{\partial z} = g_\theta - \frac{1}{\rho} \cdot \frac{\partial p}{\partial \theta} \quad (2.2)$$

$$\frac{\partial u_z}{\partial t} + u_r \cdot \frac{\partial u_z}{\partial r} + \frac{u_\theta}{r} \cdot \frac{\partial u_z}{\partial \theta} + u_z \cdot \frac{\partial u_z}{\partial z} = g_z - \frac{1}{\rho} \cdot \frac{\partial p}{\partial z}$$

Assuming axially symmetric and steady flow, some terms can be dropped, and we get the simplified Euler equations given in Equation 2.3.

$$\begin{aligned}
u_r \cdot \frac{\partial u_r}{\partial r} - \frac{u_\theta^2}{r} + u_z \cdot \frac{\partial u_r}{\partial z} &= -\frac{1}{\rho} \cdot \frac{\partial p}{\partial r} \\
u_r \cdot \frac{\partial u_\theta}{\partial r} - \frac{u_r \cdot u_\theta}{r} + u_z \cdot \frac{\partial u_\theta}{\partial z} &= 0 \\
u_r \cdot \frac{\partial u_z}{\partial r} + u_z \cdot \frac{\partial u_z}{\partial z} &= g_z - \frac{1}{\rho} \cdot \frac{\partial p}{\partial z}
\end{aligned} \tag{2.3}$$

## 2.4 Boundary Layers

When a fluid flows past a solid body, there will be a region close to the body where the flow is affected by the body's presence. This region is known as the *boundary layer*. Outside of the boundary layer, the flow can be assumed to be inviscid, whereas inside the boundary layer, viscous effects will, by the definition of boundary layers, be non-negligible [11]. As an example, Fig. 2.3 illustrates the boundary layer development of an oncoming flow being disturbed by a flat plate.

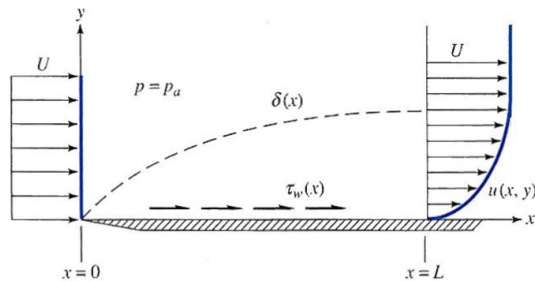


FIGURE 2.3: Example of a Flat-plate boundary layer. Note how the flow outside of the dashed line is yet unaffected by the plate's presence [13].

At the wall interface, a *no-slip* condition is assumed, meaning that the flow is assumed to have zero velocity in contact with the wall. As one moves gradually into the flow, the fluid's speed will approach the *free stream velocity*, the velocity in the inviscid region.

## 2.5 Flow separation

In addition to the retardation of the flow along the wall, the expanding draft tube cone will cause an adverse pressure gradient, and the expansion itself may give rise to flow separation [11].

The increasing downstream pressure will slow the flow, and the retarded boundary layer along the wall may experience a negative flow rate, depending on the pressure gradient. Applying the momentum equation at the wall, we get Equation 2.4, which indicates that the curvature of the velocity profile at the wall has the same sign as the pressure gradient [11]. If this pressure gradient is positive in the streamwise direction, it is known as an *adverse pressure gradient*.

$$\left. \frac{\partial^2 u}{\partial y^2} \right|_{y=0} = \frac{1}{\mu} \cdot \frac{dp}{dx} \quad (2.4)$$

As the flow progresses along an adverse pressure gradient, the velocity profile close to the wall will become more and more S-shaped, until the velocity close to the wall becomes negative, illustrated in Fig. 2.4 [11].

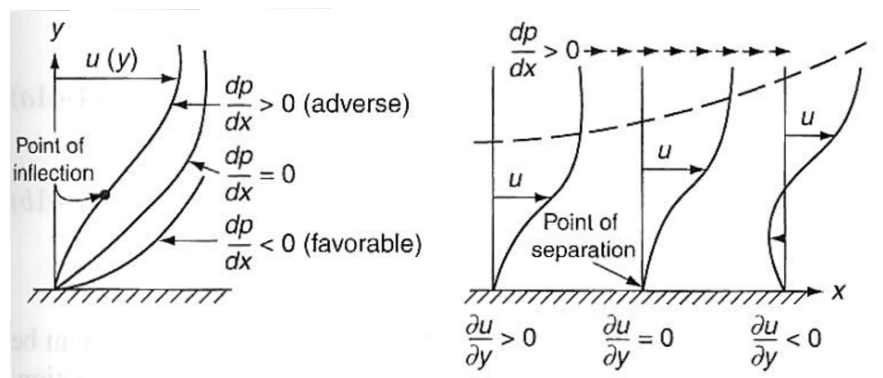


FIGURE 2.4: Pressure-driven flow separation. The adverse pressure will slow the flow close to the wall, causing negative flow [11].

Flow separation will reduce the effective divergence of the draft tube, as illustrated by Fig. 2.5, and thereby reduce the pressure recovery in the draft tube.

By introducing rotation to the flow, it has been found that the centrifugal forces acting on the water will overcome the adverse pressure gradient provided by the

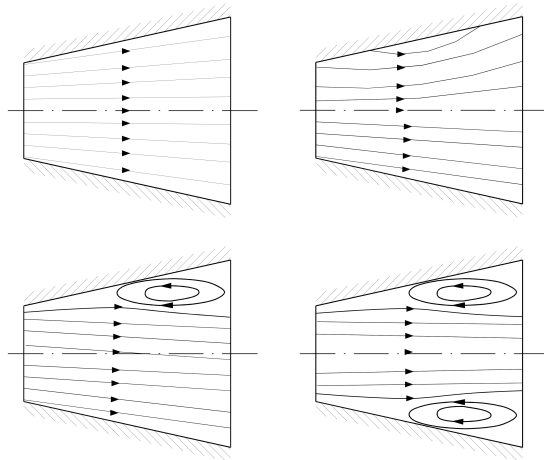


FIGURE 2.5: Reduced divergence in draft tube due to flow separation. The recirculating regions close to the wall reduce the effective increase in area of the draft tube cone [12].

boundary layer, preventing flow separation, and thereby enhancing the pressure recovery coefficient [8].

## 3 | Lab Preparation

### 3.1 HSE: lab safety

In order to use laser technology for experiments, an extensive risk assessment report had to be filled out. This report consisted of reviewing safety hazards in both the laboratory and in the procedures.

The complete HSE report has been submitted to the HSE-coordinator for the department of Energy and Process engineering at NTNU.

### 3.2 Experimental Setup

Due to HSE reasons, the complete laser setup was placed inside a black tent made of a tarp-like fabric, in order to isolate the rest of the lab from renegade laser rays.

The tests were performed at the Waterpower Laboratory at NTNU by Kaveh Amiri, Carl Bergan, and Joel Sundström. The Francis test rig was set up for running in a closed loop, where the upstream pressure can be freely regulated, and the downstream pressure can be regulated between close to atmospheric pressure and down to approx. 9 m below ambient pressure. A sketch of the test rig is provided in Fig. 3.1.

The runner in use during the measurements is a 1:5.1 scaled model of the Tokke hydropower plant. The full scale unit is a 1.78 m diameter Francis runner with a

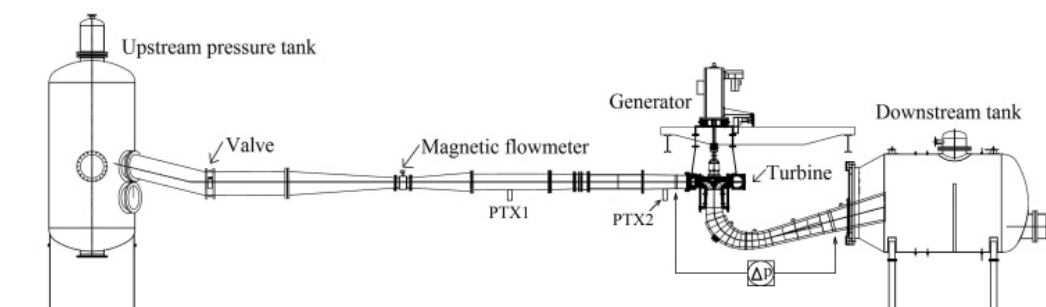


FIGURE 3.1: Sketch of the closed loop test rig [14].

nominal head of 377 m with a power of 110 MW. The distributing unit consists of a spiral casing with 10 stay vanes and 28 guide vanes. The runner has 15 full length vanes and 15 splitter vanes. The flow rate, measured by an electromagnetic flow meter, is controlled by the head upstream.

The laser used was a Spectra-Physics Model 177G. The LDA data was processed with a Burst Spectrum Analyzer (BSA) from Dantec Dynamics. The data sheet for the laser can be found in Appendix A.

The laser probe was mounted on a three-axis traverse table which allowed for accurate movement of the laser probe, and allowed for whole velocity profiles to be recorded without the need for constant attention from the operators. Since the whole laser setup was inside a closed tent, a web camera was mounted near the draft tube cone to monitor the progress from the control room in the lab. A glass prism was also mounted around the Plexiglas draft tube cone, in order to correct for the rarefaction of the laser light, and the space between the glass and the Plexiglas was filled with water.

The front lens had a focal length of 310 mm. The seeding particles used were of the type Expancel 46 WU 20 with an average diameter of 6  $\mu\text{m}$ .

Test were carried out at three operating points: part load, BEP, and full load. The corresponding operating conditions are given in Table 3.2.

In order to phase resolve the results, the runner RPM was recorded on a separate computer in addition to being recorded on the BSA. For this, two input modules

were used. One NI 9239 4-Ch  $\pm 10$  V 24-Bit Simultaneous Analog Input, and one NI USB-6211 16-Bit, 250 kS/s M Series Multifunction DAQ.

### 3.2.1 Measuring positions

Fig. 3.2 shows the two sections along which the radial velocity profiles were measured in the draft tube cone. Section I is located 64 mm below the draft tube inlet, and section II is located 382 mm below the draft tube inlet. The radius at section I and II is 177.5 mm and 196.2 mm respectively.

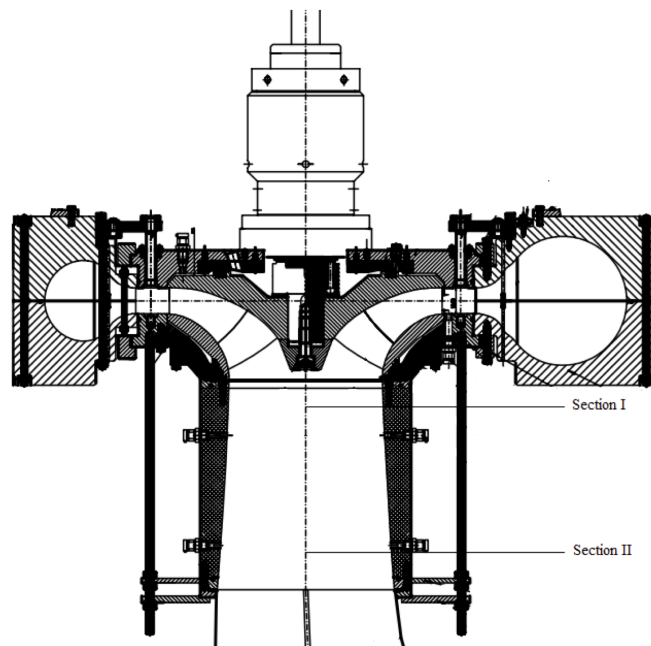


FIGURE 3.2: Measuring sections in the draft tube cone [15].

At full load and BEP, 16-17 points along the radius were measured, whereas for part load, 25-26 points were recorded. The higher number of measurement points at part load were chosen in order to better resolve large velocity gradients expected at this operating point.

### 3.2.2 Compensations due to weak laser

Several attempts were made to adjust the optics in the Bragg cell in order to achieve as much power as possible from the four laser components. This was

controlled by using an intensity meter, which in every case showed that the blue laser was considerably weaker than the green one.

Past experience with LDA at the Waterpower Laboratory shows that the blue laser will always be weaker than the green one. Due to this, and some initial measurements, it was decided that the blue laser was unfit for reliable measurements, and all the velocity profiles (tangential and axial components) had to be measured with the green laser. Implications of this are discussed in Chapter 6. Since the laser alignment was considered to be more sensitive than the repeatability of the Francis rig, the laser probe was only rotated once, meaning that all the axial velocity profiles had to be recorded before rotating the probe and then recording all the tangential velocity profiles.

### 3.2.3 Shaft encoder

There is a piece of equipment for the Dantec BSA system called a *shaft encoder*. The BSA has the option to take analogue inputs, and with the shaft encoder, this analogue input can be used to calculate the angular position of the turbine runner and perform predefined actions. This can be used to measure the velocity in between the turbine blades, as the BSA can trigger data acquisition on predefined runner angles.

In our case, the shaft encoder would be particularly useful in recording the angular position of the runner at each data point. Since the BSA used in this thesis wasn't equipped with a shaft encoder, a makeshift system had to be constructed.

The problem we faced with using the analogue channels, was that the BSA would only record voltage from the analogue input when a particle passing was recorded, thus making it impossible to accurately predict the runner position.

Attached to the runner shaft, there is a slotted disk (with one slot) and an optic sensor, which gives of 5 V when detecting the slot, and 0 V otherwise. This sensor is used in the normal laboratory setup to calculate the number of Rotations Per



Minute (RPM) for the runner. The signal from this was fed into one of the BSA analogue channels. However, given the random nature of particle passings, there is no way of being sure that the optic sensor is giving off a voltage at the arbitrary time when the BSA records data.

This challenge was overcome by attaching white tape on half the runner shaft, black tape on the other half, and mounting an optic sensor close to the tape. This sensor recorded 5 V for half the revolution and 0 V for the other half, thus maximizing the chance of successfully recording each revolution. Given a data rate of 800 particles per second, and a runner frequency of 6.77 Hz, each particle is recorded in a window of approximately  $3.5^\circ$ , giving an idea of the uncertainty in the measured angle. In order to obtain a higher resolution in the results, this voltage was recorded in parallel on a computer with a much higher logging rate (around 6 kHz), and then the angular position of the runner could be reconstructed in the post processing.

In order to facilitate the synchronization of these two signals, a single pulse was recorded on a separate channel at the beginning of each measurement series. Matching the pulse from the two computers revealed how far along the time scale the other pulses had to be shifted in order to line up properly.

### 3.2.4 Optical alignment

When working with optics, angles are important, and misalignment can reduce the data value. It was therefore paramount to ensure that the traverse table was parallel to the glass, that the laser was perpendicular to the glass, and that the laser beams were properly aligned in the vertical and horizontal direction.

For the measurements to be accurate, the laser had to hit the glass as perpendicularly as possible, and the movement axis of the traverse needed to be as perpendicular to the glass as possible. Additionally, the two laser colors had to be as close as possible to the horizontal and vertical for the tangential and axial measurements respectively.

The latter part of the alignment was performed by attaching the probe on its 'holding piece' and clamping that on a table. The table was made horizontal and the laser was fired at a wall a distance away. The probe was then rotated until the two horizontal dots were indeed level.

The next step was to attach the aforementioned 'holding piece' correctly onto the traverse table. For this, a right-angled metal piece was used. After that, aligning the traverse table with respect to the glass wall was done using the laser reflection off the glass. A control of the alignment was performed using two long pieces of flat metal with a right angle at the end, to ensure that the traverse table was indeed perpendicular to the glass wall.

### 3.3 Experimental Method

In order to make sure that the coordinate system was correct, the wall had to be located for each measurement. This was simply done by running a small recording series around where the wall was assumed to be (by visual inspection), and setting  $x=0$  where the velocity abruptly changes from 0 to a physical value, and where the velocity histogram looks even. This can be seen in Fig. 3.3.

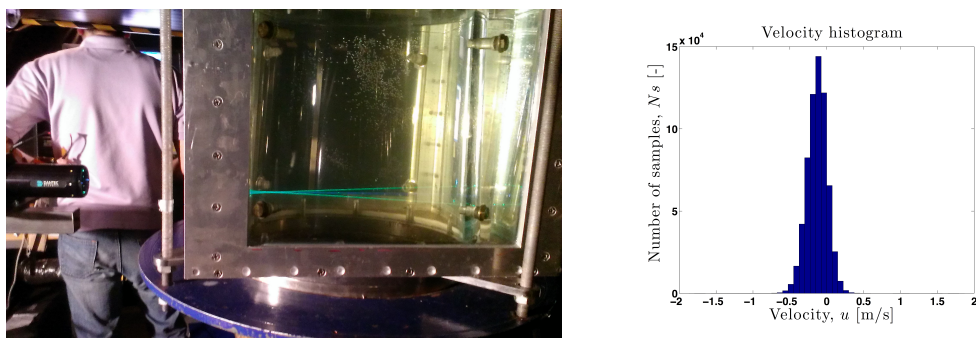


FIGURE 3.3: Finding the wall. The histogram illustrates the distribution of the measured velocity.

The measurement time for each coordinate is dictated by the number of data points required for a reliable measurement, and by the time available at the lab. It goes without saying that a large data rate will reduce the time required here. The measurement time was set to 12 minutes for most measurements, and then

reduced to 10 minutes for the last few velocity profiles, due to limited laboratory time.

### 3.4 Operating Conditions

The operating points used are described on the Francis-99 website, and they yield the test conditions described in Table 3.1.

<b>Operating point</b>	<b>H [m]</b>	<b>Q [m<sup>3</sup>/s]</b>	<b>n [Hz]</b>	<b>n<sub>ED</sub></b>	<b>Q<sub>ED</sub></b>	<b>η [%]</b>
BEP	11.91	0.203	5.59	0.18	0.15	92.6
Full load	11.84	0.221	6.16	0.20	0.17	90.6
Part load	12.29	0.071	6.77	0.22	0.05	71.7

TABLE 3.1: Francis-99 operating conditions [14].

Upon reaching these operating points, the generator exhibited instabilities which resulted in an unacceptable variation in torque and RPM. This was observed for both full load and BEP, not for part load. It was deemed best to perform the measurements on a slightly different operating point, maintaining constant  $n_{ED}$  and  $Q_{ED}$ , but altering the head slightly.

After some experimentation, it was decided upon substituting full load and BEP with the test conditions shown in Table 3.2. Implications of the change in operating conditions are discussed in Chapter 6.

<b>Operating point</b>	<b>H [m]</b>	<b>Q [m<sup>3</sup>/s]</b>	<b>n [Hz]</b>	<b>n<sub>ED</sub></b>	<b>Q<sub>ED</sub></b>	<b>η [%]</b>
BEP	12.77	0.207	5.74	0.18	0.15	92.4
Full load	12.61	0.230	6.34	0.20	0.17	91.0
Part load	12.30	0.071	6.77	0.22	0.05	72.5

TABLE 3.2: Operating conditions used in this thesis.



## 4 | Data analysis

The data obtained from the BSA comes in the form of a text file, with columns for each data type. Post processing the data is, for the most part, a trivial issue. The challenge in this test was the absence of a shaft encoder, as mentioned in Chapter 3.

The analysis consists of matching two pairs of square waves: the wave consisting of the starting pulse marking the beginning of each logging series, and the wave consisting of each runner revolution. These were matched together using cross correlation in an iterative fashion.

The logging equipment used has discrete logging rates, but when recording the waves in SignalExpress, a rate of 6 kHz was chosen. This gave rise to erroneous time steps, creating the need for iterative cross correlating.

### 4.1 Waveform coupling

The purpose of the square waves was to provide some means of reconstructing the angular position of the runner in retrospect. However, matching the high-resolution square wave with the (relatively) low resolution velocity measurements requires some numerical analysis.

### 4.1.1 Logging rate

According to the online data sheet for the NI 9239 module [16], the logging rates for this particular input module is calculated by Equation 4.1.

$$F_s = \frac{f_M \div 256}{m}, \quad m = 1, 2, \dots, 31 \quad (4.1)$$

where  $f_M = 12.8$  MHz for the NI 9293.

Since data acquisition was set at a different logging rate than what the logging card can provide, it was assumed that the logging card used a logging rate close to the chosen one, given by the available logging rates. This was used as a 'best guess' for the logging rate in the iterative cross correlation of the square waves in order to save on computing time<sup>1</sup>.

The BSA records data at random time intervals, but provides a time stamp for each recorded data point.

### 4.1.2 Cross correlation

Cross correlation is a measure of the similarity of two wave forms as a function of the time-lag applied to them. Mathematically, it is defined for continuous functions  $f$  and  $g$  as

$$(f \star g) = \int_{-\infty}^{\infty} f^*(t) \cdot g(t + \tau) \cdot dt \quad (4.2)$$

where  $f^*$  denotes the complex conjugate<sup>2</sup> of  $f$  and  $\tau$  is the time lag [17].

The cross correlation will give a good estimate as to how far the data has to be shifted on the time scale to get the best match. This was used in the iterative

---

<sup>1</sup>If the actual logging rate was outside of this range, it will still be found, but the computing time will be significantly longer.

<sup>2</sup>For a real function, this will simply be the function itself.

cross correlation whereby the square waves were shifted relatively to each other to find the maximum correlation, and the frequencies of the waves was compared, giving a suggestion for a new time step for the recorded data.

The time stamp provided by the BSA was assumed to be correct in this procedure.

## 4.2 Phase resolving

The RVR introduces a periodic phenomena, which can be used to phase resolve the results. What this entails, is that the flow will be more or less periodic with different phenomena at different periods. The two most prominent periodic phenomena of interest here are the RVR and the rotation of the runner itself.

Keeping in mind that the velocity can be decomposed into three parts, the mean velocity, the periodically fluctuating velocity, and the randomly fluctuating velocity, it is crucial to find the periodic part in order to be able to analyze the turbulence.

The process of phase resolving the data consists of using the time stamp of the velocity measurements in order to place each velocity measurement in an appropriate 'phase bin' of an appropriate size. The size of this phase bin, or window size, depends on the phenomena of interest and should be carefully selected. The windows should be as small as possible in order to get a high resolution in the phase-averaged values, but large enough to contain enough samples such that the phase-averaged data dominate the random fluctuations. This is especially true if the flow contains large temporal gradients [18].





## 5 | Results

The complete data gathered from the experiments are far too extensive to present in this thesis. As such, only a post-processed selection of the data is presented for each operating point.

### 5.1 Velocity profiles

The velocity profiles from all the measurements are presented in this section. They are obtained by taking the time-averaged velocities for each measuring coordinate. For comparison purposes, they are presented as reduced values divided by the bulk velocity immediately downstream of the runner, shown in Equation 5.1. The radial coordinate is reduced with respect to the radius at the runner outlet,  $R = 0.175$  m. The resulting  $U_{BULK}$  is shown in Table 5.1.

$$u^* = \frac{u}{U_{BULK}} = \frac{\pi \cdot D^2 \cdot u}{4 \cdot Q} \quad (5.1)$$

The reduced velocity profiles for position I and position II are superimposed on each other for comparison purposes.

<b>Operating point</b>	<b><math>U_{BULK}</math> [m/s]</b>
Part Load	0.7375
BEP	2.1503
Full Load	2.3892

TABLE 5.1:  $U_{BULK}$  for the different operating points.

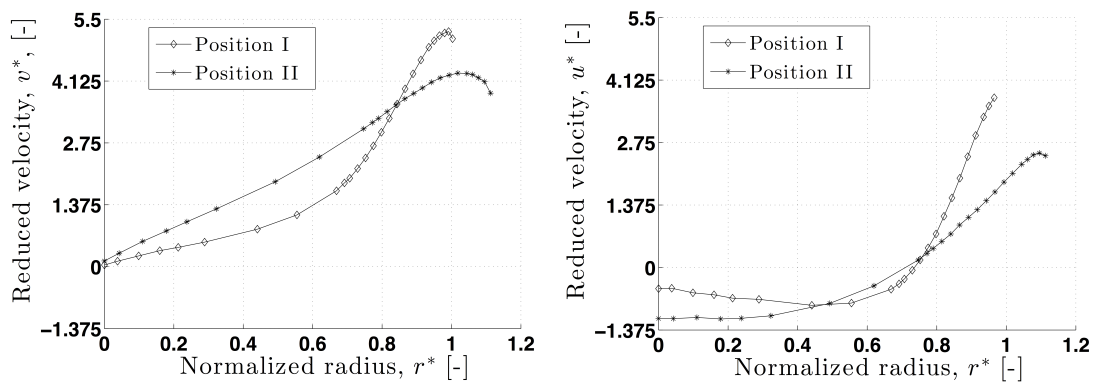


FIGURE 5.1: Tangential (left) and axial (right) reduced velocity profiles for part load.

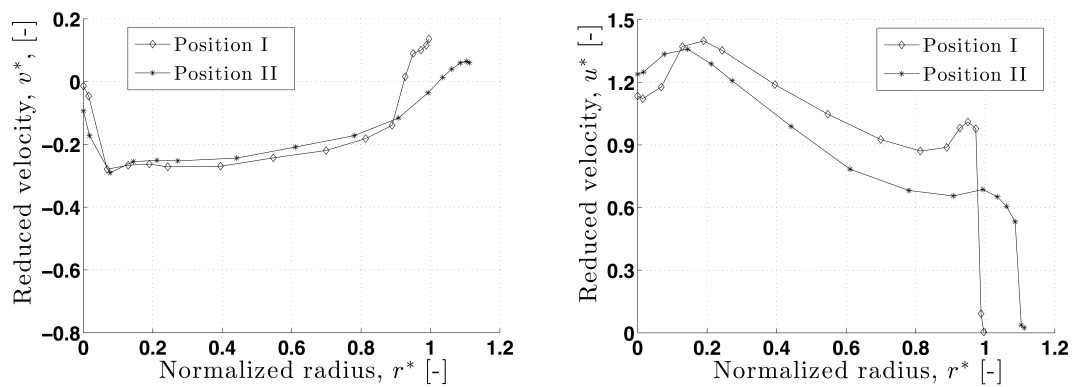


FIGURE 5.2: Tangential (left) and axial (right) reduced velocity profiles for BEP. Note the difference in vertical axes.

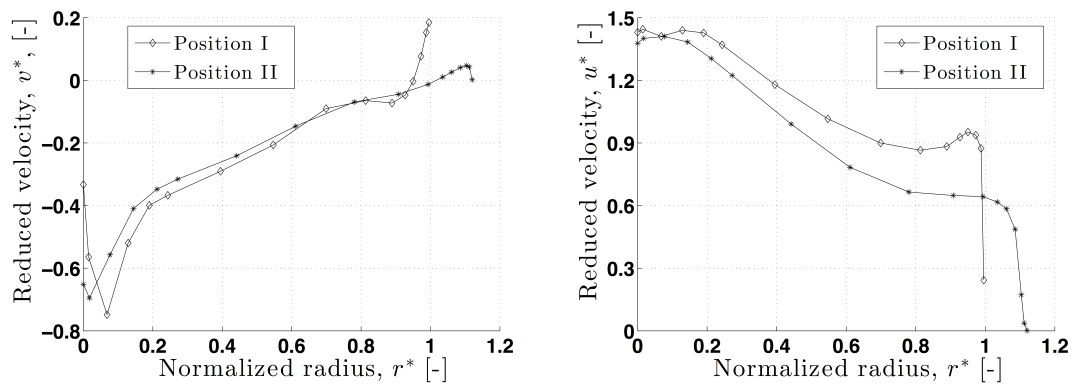


FIGURE 5.3: Tangential (left) and axial (right) reduced velocity profiles for full load. Note the difference in vertical axes.

## 5.2 Phase-averaged velocity

The phase-averaged plots visualize the flow in the draft tube cone at the different operating conditions. They are obtained by phase-averaging the measured velocities with the runner frequency. The data analysis is performed in the same way as in [15]. Note the difference in scale for the plot coloring. The results for BEP are included in this section, all the phase-averaged plots can be found in Appendix C.

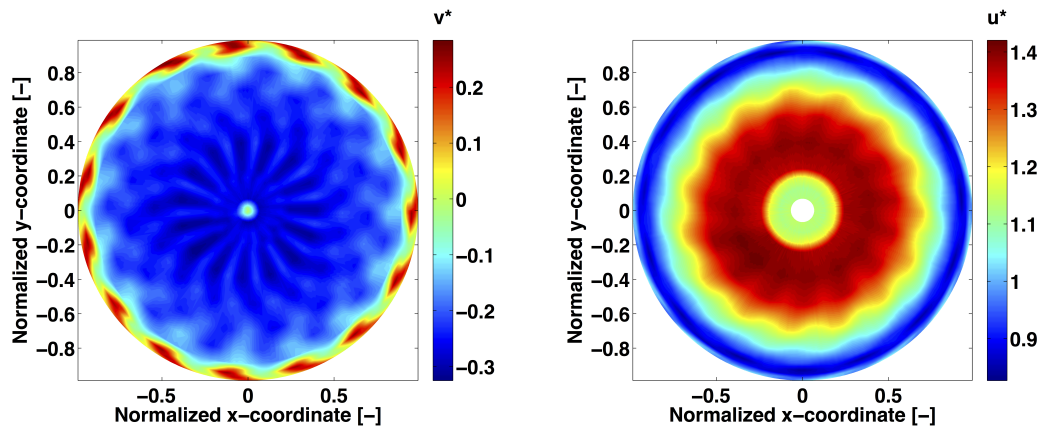


FIGURE 5.4: Phase averaged tangential (left) and axial (right) velocity for BEP, position I.

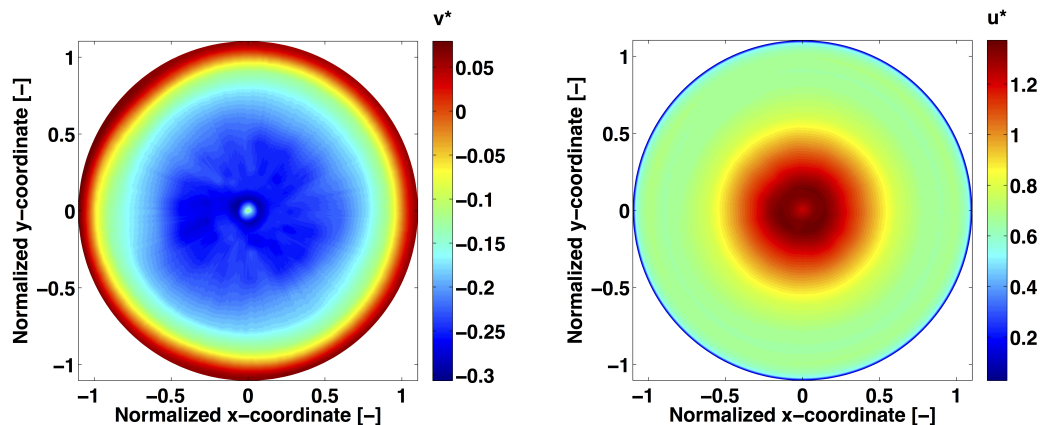


FIGURE 5.5: Phase averaged tangential (left) and axial (right) velocity for BEP, position II.

## 5.3 Turbulence

The turbulence is found by decomposing the velocity  $u(x, t)$  into three components

$$u(x, t) = \bar{u}(x) + \tilde{u}(x, t) + u'(x, t) = \langle u(x, t) \rangle + u'(x, t) \quad (5.2)$$

Where  $\bar{u}(x)$  is the time-averaged velocity and  $\tilde{u}(x, t)$  is a periodic velocity component. Combined they form  $\langle u(x, t) \rangle$ , which is the phase-averaged velocity with respect to periodic flow phenomena.  $u'(x, t)$  denotes random fluctuations in velocity, which stems from turbulence [15].

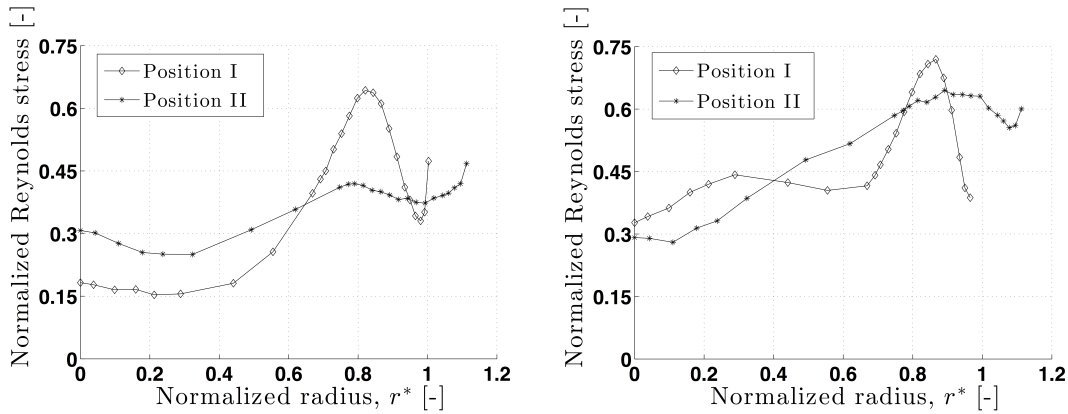


FIGURE 5.6: Reynolds normal stresses  $v'^2$  (left) and  $u'^2$  (right) for part load.

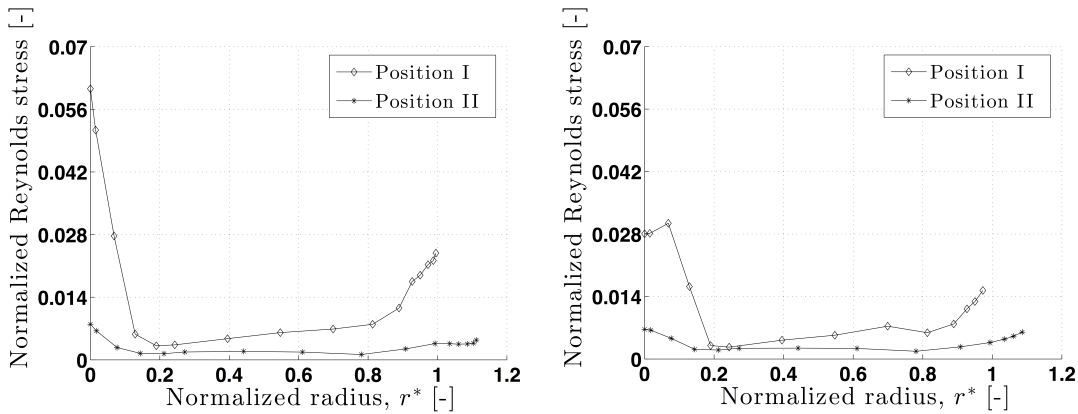


FIGURE 5.7: Reynolds normal stresses  $v'^2$  (left) and  $u'^2$  (right) for BEP.

## 5.4 CFD velocity profile comparison

The following figures show the velocity profiles obtained by LDA compared to various simulations. The figures are produced by Ruben Moritz.

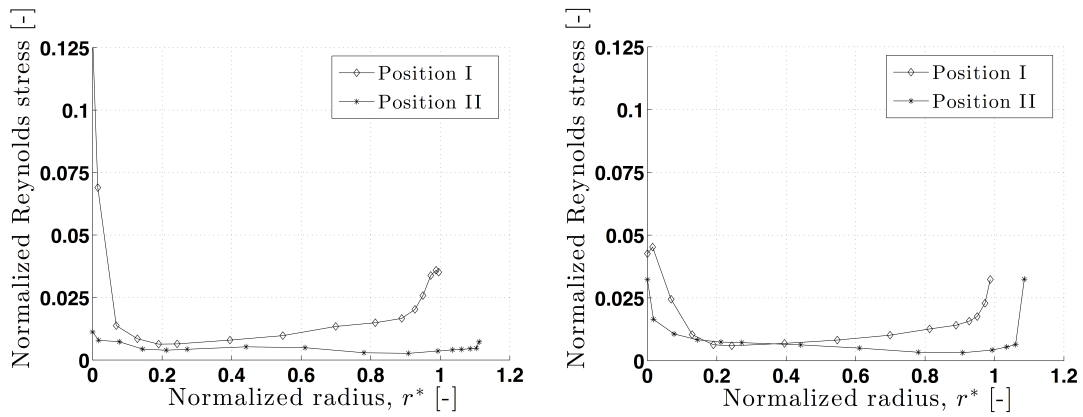


FIGURE 5.8: Reynolds normal stresses  $v'^2$  (left) and  $u'^2$  (right) for full load.

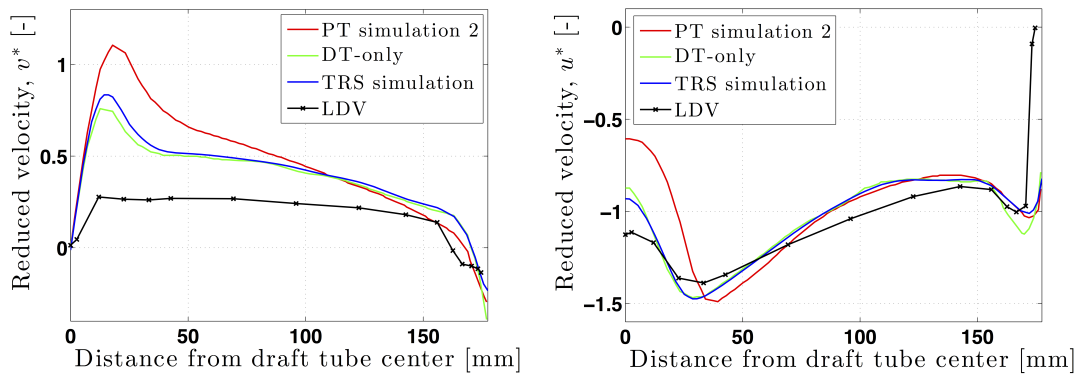


FIGURE 5.9: Tangential (left) and axial (right) reduced velocity profiles for BEP at section I produced with CFD compared with LDA results.

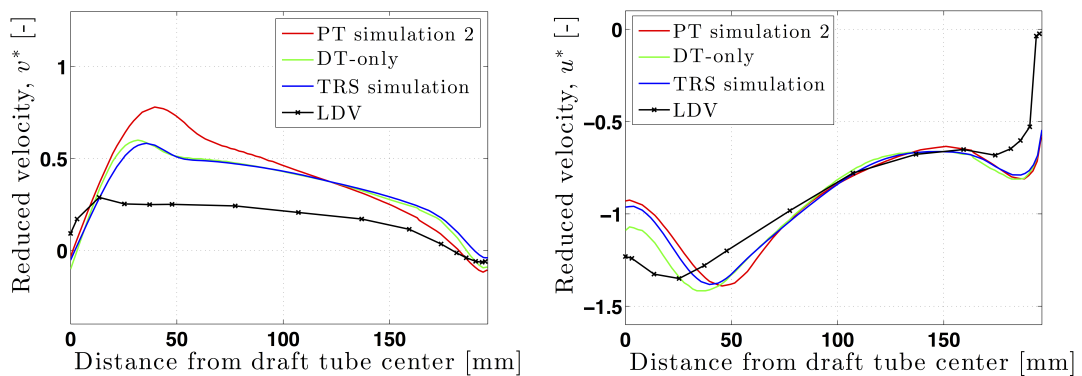


FIGURE 5.10: Tangential (left) and axial (right) reduced velocity profiles for BEP at section II produced with CFD compared with LDA results.



## 6 | Discussion

The flow field immediately downstream the runner shows distinct traces of the runner design. Further downstream, the velocity profiles are more smooth, due to the shear stresses in the flow suppressing the large gradients. The velocity profiles show a transition from the profile in Fig. 5.4 towards the flow in Fig. 6.5.

The normal Reynolds stresses were similar for full load and BEP, but were an order of magnitude greater for part load. This is most likely due to the large velocity gradients present in part load flow, and is further confirmed when the turbulence reaches a maximum at the largest velocity gradients.

### 6.1 Evaluation of the experimental setup

The experimental setup is described in Chapter 3. It is of adequate quality, and the test rig shows good repeatability. The uncertainties in the physical setup is thought to manifest itself in uncertainties in the turbulence and, to some degree, in the radial coordinate. The velocity profiles and phase-averaged values are not affected significantly by uncertainties in the laboratory setup.

#### 6.1.1 Repeatability of the Francis rig

As mentioned in Chapter 3, the axial and tangential components of the velocity had to be recorded at different times. In order to ensure that the operating point

	<b>Part load</b>	<b>BEP</b>	<b>Full load</b>
<b>Recorded efficiencies [%]</b>	72.11	92.57	90.94
	72.12	92.30	90.99
	71.71	92.41	90.91
			91.13
<b>Mean efficiency [%]</b>	71.98	92.43	90.99
<b>Repeatability [%]</b>	$\pm 0.27$	$\pm 0.14$	$\pm 0.14$

TABLE 6.1: Repeatability of the Francis rig. The efficiencies are calculated as the mean of a 2 minute series.

recorded was indeed the same, a 2 minute series were recorded for each velocity profile, and the measurements for the same operating point were then compared.

In comparing the files, the time-averaged values were calculated, outlying data points were removed<sup>1</sup>, and the relative difference between the two logging files was calculated. This simple analysis showed that, even though the conditions were not exactly the same for all the parameters, they were within acceptable limits.

The variations in hydraulic efficiency are shown in Table 6.1.

### 6.1.2 Sources of errors

The experimental setup is subject to a number of sources of errors in the measurements, which can be classified as random and systematic errors. Many of the error margins for systematic errors are supplied by the equipment manufacturer, and are relatively small. In evaluating the laboratory setup, differentiating between random and systematic errors is important in order to evaluate the data quality. Systematic errors can be corrected for retrospectively<sup>2</sup>, but this is not the case for random errors. The different sources of errors affect the results in different ways,

<sup>1</sup>Data points that differ greatly from the mean, due to obvious logging errors, e.g., efficiency of  $3 \cdot 10^8$ .

<sup>2</sup>Given that it is known how the systematic error affects the data, e.g., the distance of a misalignment or the error in a sensor zero point.



and to different degrees. Turbulence is concluded to be the most sensitive result with respect to the following sources of errors.

### **Alignment of laser**

Optical misalignment is a systematic error with a potentially large impact on the data quality. Much effort was therefore put into properly aligning the equipment, as described in Chapter 3. The laser probe's perpendicularity with respect to the glass wall is considered to be satisfactory, as the alignment was double checked using the glass wall as a mirror while the laser probe was a distance away. Using this method, one can ensure precise alignment.

When the equipment was properly aligned, the fastening bolts were tightened, ensuring no relative movement of the equipment during the measurements.

### **Movement of traverse table**

When recording each velocity profile, the wall had to be found by measuring the velocity in the vicinity of where the wall was thought to be, shown in Fig. 6.1.

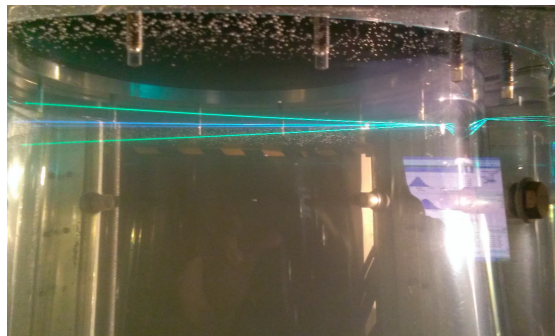


FIGURE 6.1: Locating the draft tube wall.

The coordinate for the wall seemed to change slightly between velocity profiles, meaning that there had been a relative shift of the traverse table. This change was in the order of millimeters, approximately 1 mm to 3 mm for a 12 minute measurement, so it should not introduce unacceptable errors in the velocity profiles measured. Movement of the traverse table would cause some uncertainty to the

coordinate of the measured volume, an uncertainty which is greater as one moves towards the center of the draft tube cone. This is particularly crippling for the results in the presence of large velocity gradients, such as for  $r^* = 0.8$  at part load (shown in Fig. 5.1).

Other than that, this movement would not have a significant impact on the quality of the results.

## **Calibrations**

The calibration reports for the generator torque, the friction torque, flow rate, differential pressure, and inlet pressure are included in Appendix B.

## **Instabilities**

The turbine exhibited instabilities in the generator torque when operated in BEP and at full load. The variation in generator torque was around  $\pm 50$  Nm when the generator torque was around 600 Nm. This particular instability was noticed by visual inspection of the torque history data in the control room.

Since no other instabilities could be found by visual inspection of the graphs, potential instabilities are considered to be insignificant to the measurements. The error caused by instabilities introduces periodic phenomena of unknown frequencies, which reduces the quality of the phase-resolved data. This, in turn, reduces the credibility of the measured turbulence, since it is directly linked to the periodic velocities, as seen in Equation 5.2.

## **Vibration**

The Francis rig, being a piece of rotating machinery, is subject to vibrations of a number of frequencies. Vibration can cause relative movement between the whole rig and the laser probe. This was not counteracted to a great extent in the

measurements, partly because they were considered to be insignificant, and partly because there is not much one can do about it.

The traverse table was placed on a pallet (to raise it from the floor), which has some internal dampening of vibrations, but not much. The challenge here is that the floor the traverse was placed on is not directly connected to the test rig. The draft tube and spiral casing are mounted on beams attached to the walls, and most vibrations will be dampened when traveling through the building. If the traverse table was somehow connected to the draft tube cone or to the spiral casing, this might introduce vibrations that would excite the traverse table, creating further errors in the measurements.

The setup is therefore considered to be adequate with respect to vibrations. The error in this would cause erroneous measurements in turbulence, as this is the part of the measurements that is most sensitive to vibrations.

### **Back scattering**

As mentioned in Chapter 3, the BSA was recording in back scattering mode. This method of recording greatly simplifies the experimental setup, both due to the laser emitter and recording probe being one single unit, and because one doesn't need to correct for the refraction of the laser light when exiting the draft tube cone at an off-angle.

The disadvantage with back scattering is that the amount of light scattered back towards the laser emitter is much less than that which could have been captured with forward scattering. This is due to the intensity variation of light scattered of spherical surfaces [19], and will not be discussed further in this thesis.

## 6.2 Choice of operating point

Upon reaching the desired operating conditions, the generator exhibited torque-related instabilities in both BEP and full load operation. In order to avoid undesired disturbances from these instabilities in the results, the test were performed at a different head, while keeping  $n_{ED}$  and  $Q_{ED}$  constant. A sensitivity analysis was performed by measuring the velocity for a short amount of time in both the unstable area and in our chosen operating point. The resulting velocity profiles are shown in Fig. 6.2.

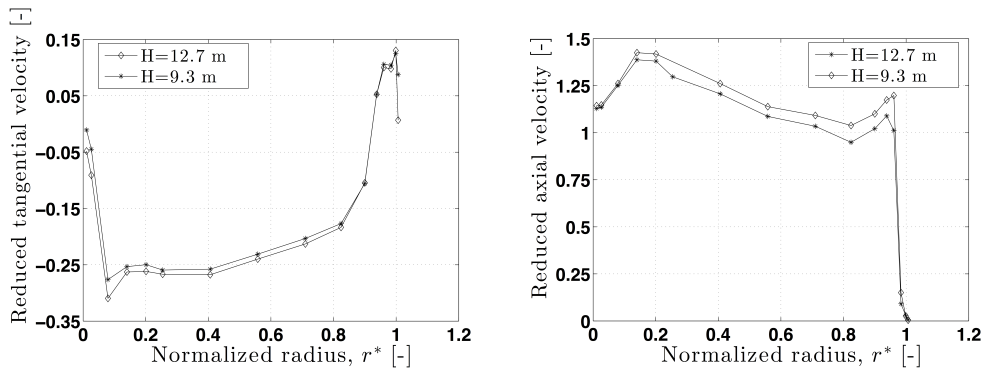


FIGURE 6.2: Reduced tangential (left) and axial (right) velocities for the compared operating points.

The sensitivity analysis shows that even though the velocity won't be exactly the same at this different pressure, it is still close enough and similar enough to be of help when performing numerical simulations of the runner, and the measurements are therefore considered admissible for the Francis-99 workshop.

## 6.3 Flow properties

Looking at the velocity profiles for the same operating point but different measuring positions, the effect of the draft tube cone is clearly shown. This can also be seen in the phase resolved plots: the oscillations are damped downstream the draft tube cone, and the flow approaches a Rankine Vortex, as discussed in Chapter 2.

The viscous boundary layer can easily be seen in the axial velocity profiles for BEP and full load. In part load operation, the large tangential velocity forces water towards the wall, creating a large pressure gradient. The low flow rate is dominated by the adverse pressure gradient in the draft tube cone, causing a zone of negative flow in the center of the draft tube.

By close inspection, the velocity profile for part load operation does seem to exhibit some wall effects, a reduction of the axial and tangential velocity in the vicinity of the wall. This agrees (for the tangential part) with the theory of the Rankine Vortex. It is, however, a relatively small reduction in velocity when compared to the magnitude of the part load velocity profile.

One can also see that the flow field starts from a forced velocity distribution created by the runner and approaches a more natural velocity profile shown in Fig. 6.5. It is reasonable to assume that a longer straight tube would let the flow approach this flow pattern.

There is also some rotation in the draft tube at BEP operation. This is usually induced in order to improve upon the draft tube pressure recovery [8].

### 6.3.1 Flow profile similarities

The velocity profile for full load operation and BEP are almost identical, but the velocity profile for part load operation is substantially different. All the velocity profiles approach a Rankine Vortex to some degree, with the location of the maximum velocity shifted in the radial direction. The tangential flows seem relatively unchanged through the draft tube cone, the only change being in magnitude and that it's a bit smoother further down from the runner.

By comparing the reduced velocity profiles for each operating point at the same position, the similarity between the operating points become more clear. The reduced velocity profile for BEP and full load are almost identical, whereas the reduced velocity profile for part load is drastically different. For part load operation, the large tangential component of the velocity will force water out towards

the draft tube wall, creating a large pressure gradient which will dominate the flow field close to the wall. This also contributes to a large kinetic energy, accounting in large for loss of hydraulic efficiency at part load.

As the water moves down the draft tube cone, the effects of the runner diminish and the flow approaches a more typical rotating pipe-flow.

### 6.3.2 Back flow: The dead core

As seen in the velocity profiles for part load operation, there is quite a large region of axial flow with negative velocity. The high rotational speed in part load operation creates a large pressure gradient when approaching the wall. At part load operation, the flow rate is low, but the rotational velocity is staggeringly high. Revisiting Equation 2.3, and assuming that the low flow rate causes the radial velocity,  $u_r$ , to be negligibly low when compared to  $u_\theta$ , Equation 2.3 can be reduced to Equation 6.1:

$$\frac{u_\theta^2}{r} = \frac{1}{\rho} \cdot \frac{\partial p}{\partial r} \quad (6.1)$$

The rotation forces water out to the wall, preventing a back flow scenario along the wall that is commonly associated with expanding flows in adverse pressure gradients [11]. This will, according to Equation 6.1, leave the flow with a very high pressure along the wall. Evaluating the z-component of Equation 2.3, and assuming positive z-direction in the flow direction, the terms of the equation take on the following:

$r^*$ -range	$g_z$	$u_z$	$\frac{\partial u_z}{\partial z}$	$\frac{\partial p}{\partial z}$
0.0 – 0.5	$> 0$	-1.125	-2.09	$> 0$
0.5 – 0.8	$> 0$	$< 0$	$> 0$	$> 0$
0.8 – 1.0	$> 0$	$> 0$	$< 0$	$> 0$

TABLE 6.2: Axial pressure gradients in the draft tube cone. The values for  $r^* = 0 - 0.5$  are taken as approximate values from Fig. 5.1.

Solving for the pressure gradient, we get Equation 6.2

$$\frac{1}{\rho} \cdot \frac{\partial p}{\partial z} = g_z - u_z \cdot \frac{\partial u_z}{\partial z} - u_r \cdot \frac{\partial u_z}{\partial r} \approx g_z - u_z \cdot \frac{\partial u_z}{\partial z} \quad (6.2)$$

Thus, there is a positive pressure gradient in the flow direction for the whole cross section of the draft tube cone. The large radial pressure along the wall will force the water towards the center, and with the positive pressure gradient in the flow direction, the flow rate is too low to overcome this obstacle, causing back flow in the draft tube center. This phenomena is illustrated in Fig. 6.3.

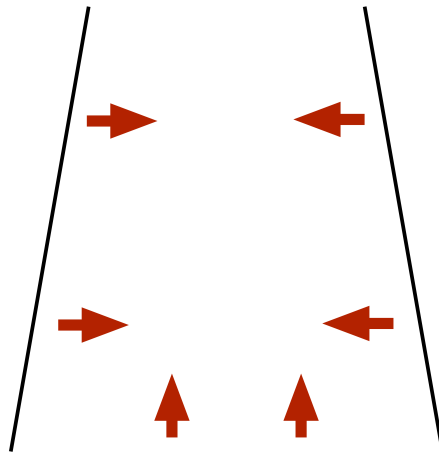


FIGURE 6.3: Direction of decreasing pressure in the draft tube. The pressure gradients indicate where the water is forced by the pressure.

This region of back flow is accompanied by an increase in the water velocity close to the wall, since the entire flow rate plus the recirculated water must pass through that area. This is likely one of the reasons for the lower efficiency at this operating point.

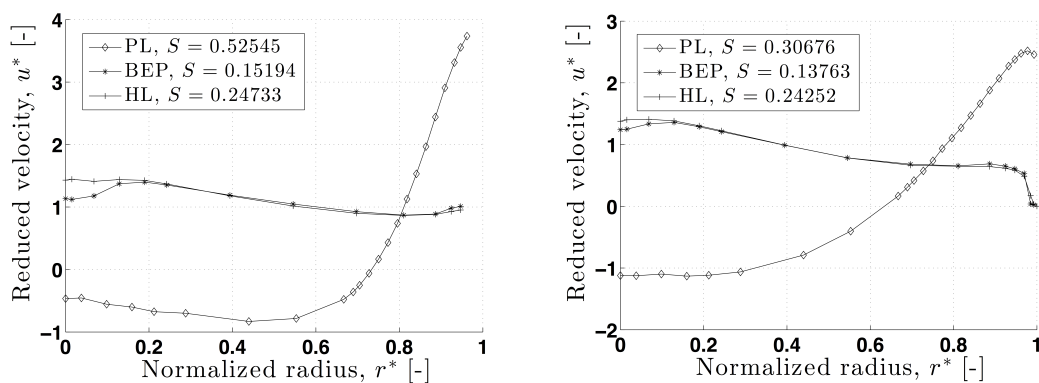


FIGURE 6.4: Reduced velocities for position I (left) and position II (right) at different swirl numbers.

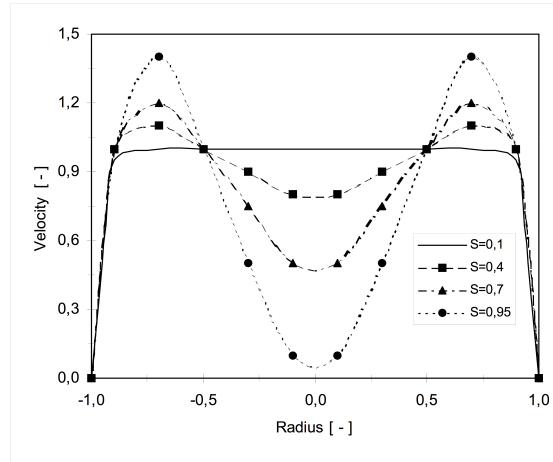


FIGURE 6.5: Axial velocity for swirling flow at different swirl intensities [3].

From Fig. 6.4 we see that the velocity changes from position I to position II are in the direction of the flow illustrated in Fig. 6.5, and that the retardation has occurred mainly along the draft tube wall.

For BEP and full load operation, the turbine's design provides a high flow in the center region of the draft tube cone, preventing back flow. The flow immediately downstream the runner will be dominated by the runner design, before it reverts towards a Rankine Vortex further downstream. As the cross section area increases, the axial velocity will decrease, and without a large axial velocity, there is a real possibility that the axial velocity will drop below zero. This phenomena is often dubbed Vortex Breakdown [3]. The region of high axial velocity immediately downstream the runner may in this way prevent the formation of a dead core with back flow further downstream, which in turn will increase the turbine performance.

### 6.3.3 The Rankine Vortex

When moving downstream, the tangential velocity profiles exhibit a shift from the forced velocity profiles generated by the turbine, towards a Rankine Vortex.

For part load, transition can be seen in the reduction of the largest velocity gradient around  $r^* = 0.9$  and the following increase in the velocity gradient from  $r^* = 0$  to  $r^* = 0.5$ . It is likely that, if not for the bend in the draft tube, the peak tangential



velocity would move in towards the center of the draft tube further downstream, allowing for a free vortex outside of the solid body rotation zone.

The tangential velocity profile for full load and BEP have similar properties, a forced velocity profile in position I due to the runner, and a similar transition as for part load. Large gradients are reduced, particularly the gradient in  $r^* = 0.9-1$ .

For BEP, the velocity profile in position I is for the most part a constant velocity profile, with some changes at the wall and at the draft tube center. Further downstream, this profile shifts towards a solid body rotation, with some wall effects distinguishable close to the wall. It is therefore reasonable to assume that the tangential velocity profile for BEP will approach a Rankine Vortex further downstream.

For full load, the velocity profile shifts towards a solid body rotation with small effects of the wall near  $r^* = 1$ . This is due to the tangential velocity being close to zero near the wall already.

### 6.3.4 Blade wakes

Fig. 5.4 shows the phase averaged data for BEP from the LDA measurements, and it clearly illustrates the velocity field in the draft tube cone, as well as showing the effects of the runner blades. We see how the velocity drastically increases towards the middle, and how greatly it depends on the runner blades, causing pressure pulsations. These pulsations will cause fatigue loads to the runner, and in some cases, unacceptable power swings.

Wakes from the runner blades can be seen in some of the phase averaged plots. In particular for BEP operation, shown in Fig. 5.4, the phase resolved tangential velocity immediately downstream the runner shows unmistakable traces of the runner blades.

This becomes even more clear when plotting the contours around threshold values, shown in Fig. 6.6. The runner blades can be seen in the tangential velocity for all operating points at position I.

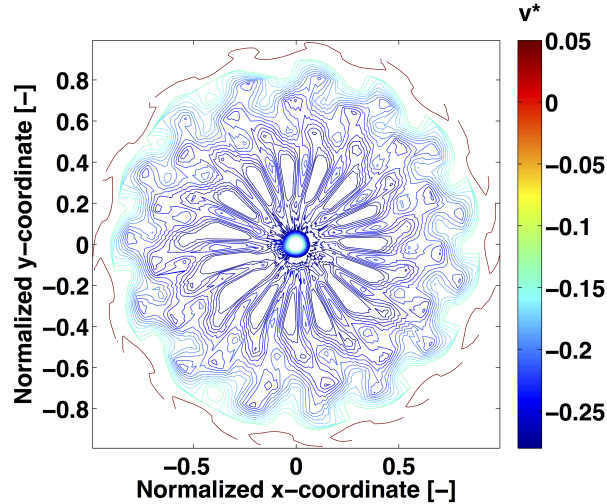


FIGURE 6.6: Contours of phase resolved tangential velocity at BEP, position I.

The tangential flow field shown at BEP in position I is in many ways the design fingerprint of the runner. It clearly shows how the water exits the turbine at the different operating points. Traces of the runner blades disperse quickly through the draft tube cone, and are no longer detectable at position II. This is due to the amount of shear introduced by these large local velocity gradients, and they will therefore even out after a relatively short time.

### 6.3.5 Turbulence

Turbulence is calculated as the normal Reynolds stresses,  $u'^2$  and  $v'^2$ . As mentioned earlier, it was only possible to calculate the normal Reynolds stresses, due to limitations in the experimental setup regarding laser strength and back scattering. In terms of using the data for simulation validation, they are sufficient, but not ideal. The graphs given in Chapter 5 give an idea as to how the expected results should be, and can be a great help in picking the correct turbulence model for numerical simulation.

For both full load and BEP operation, the Reynolds stresses appear to show significant variation only at the draft tube center and in the vicinity of the wall. The high level of stresses in the draft tube center can be explained by the chaotic nature of the flow in this position. When approaching the wall, the viscous boundary layer becomes dominant, causing large stresses on the flow.

For part load operation, the normal stresses are an order of magnitude larger than at the other operating points. There is also a maximum of stresses around  $r^* = 0.7 - 0.8$ , which is approximately at the interface between the positive and negative axial flow. This is also an area of large velocity gradients, seen in Fig. 5.1, which could contribute to the large turbulence. As mentioned earlier, there is some uncertainty in the measurement position's coordinates.

## 6.4 CFD results

Velocity profiles for BEP have been simulated by Ruben Moritz, and are shown in Fig. 5.9 and Fig. 5.10. The simulated velocity profiles show some agreement with the measured results for the axial velocity component, with the largest discrepancy occurring in the draft tube center. The tangential velocity profiles show little agreement, with an exaggerated velocity near the draft tube center. Even though the velocity magnitudes are different for the tangential velocity components, traits of the velocity profile seem to agree with the measured profile. In the CFD results, a velocity peak is clearly visible close to the draft tube center. By close inspection, a similar peak is visible in the measured velocity profile, but it is much smaller. There is reason to believe that a higher spatial resolution in the measurements will reveal a similar-looking peak in the tangential velocity profile, even though the magnitude will be much smaller.

According to Ruben Moritz, the mesh used for the simulation caused a small extension of the runner hub, artificially creating a short semi-tapered cone [20]. This would limit the axial velocity and increase the tangential velocity close to the center. This could account for some of the discrepancies in the simulated results.

---

Another theory is that the discrepancies can be attributed to the measurements for BEP were carried out at different operating conditions than those given in Table 3.1. There is reason to believe that the difference in velocity magnitude can be attributed to the difference in head and flow. However, comparing the velocity profiles in Fig. 6.2, the tangential velocity profile does not exhibit more sensitivity to a change in operating conditions than the axial velocity profile. The difference between simulated and measured velocity profiles is much greater in the tangential direction than in the axial direction, but both velocity components show little sensitivity to a slight change in operating point. Since the error seems to be limited to the tangential velocities, it can *not* be attributed to the measurements being performed at slightly different operating conditions than prescribed by Table 3.1. There is reason to believe that the discrepancies in simulated tangential velocity stems from numerical errors in the simulation, such as errors in the meshing.

# 7 | Conclusions

## 7.1 Conclusions

The velocity profiles within the draft tube of the Tokke model runner have been accurately measured, and they have been compared to the CFD results of the same runner. The measurements were carried out under satisfactory laboratory conditions, with relatively low uncertainties in the measured velocity profiles, and the measurements for turbulence show agreement with expected results. The measurements show that the Tokke runner has moderate swirl at BEP, which prevents a low-pressure region near the draft tube wall, enhancing draft tube performance. Additionally, the runner shows an increased discharge near the center of the draft tube cone, minimizing the risk of back flow. The post-processed results show distinct traces from the runner in the draft tube flow, and large normal stresses in the presence of large velocity gradients.

Comparisons with CFD results show good agreement with the measured axial velocity profiles, but large discrepancies in the tangential flow. However, some traits of the tangential velocity profile can be seen in the simulations, but the velocity magnitudes are unacceptable.

Measurements of turbine performance and pressure pulsations were not performed due to limited laboratory time.

## 7.2 Further Work

More accurate turbulence measurement could be performed with a shaft encoder installed and with the 2D probe working. 3D anemometry is recommended in order to calculate the complete Reynolds stress tensor. 3D velocimetry will also enable solving for all the terms in the Euler equations, yielding the pressure gradients in the draft tube cone, which in turn yields the pressure field in the draft tube when coupled with pressure measurements along the wall. This would also enable correlation between transient velocity phenomena and variations in pressure.

In order to better understand transient phenomena, PIV measurements should be performed in the draft tube cone. Phenomena that can be investigated with this method is the formation of the dead core, the formation of the RVR, vortex breakdown, and RVR precession frequencies.

Better agreement with simulated results and measured results could be achieved by CFD-simulation using same operating conditions as in this thesis, particularly for part load and full load. Comparisons with the measured normal stresses should also be performed.

# References

- [1] Einar Kobro. *Measurement of Pressure Pulsations in Francis Turbines*. PhD thesis, Norwegian University of Science and Technology, 2010.
- [2] Thomas Veveke. *An Experimental Investigation of Draft Tube Flow*. PhD thesis, Norwegian University of Science and Technology, 2004.
- [3] Ole Gunnar Dalhaug. *A Study of Swirl Flow in Draft Tubes*. PhD thesis, Norwegian University of Science and Technology, 1997.
- [4] Kaveh Amiri. An experimental investigation of flow in a kaplan runner: Steady state and transient, 2014.
- [5] W. Glas, M. Forstner, K. Kuhn, and H. Jaberg. Smoothing and statistical evaluation of laser doppler velocimetry data of turbulent flows in rotating and reciprocating machinery. *Experiments in Fluids*, 29:411–417, 2000.
- [6] Chirag Trivedi, Michel J. Cervantes, B. K. Gandhi, and Ole G. Dahlhaug. Experimental and Numerical Studies for a High Head Francis Turbine at Several Operating Points. *Journal Fluids Engineering*, 135(11):111102–111102, 08 2013.
- [7] Øyvind Antonesen. *Unsteady Flow in Wicket Gate and Runner with Focus on Static and Dynamic Load on Runner*. PhD thesis, Norwegian University of Science and Technology, 2007.
- [8] Yasutoshi Senoo, Nobumasa Kawaguchi, and Tetsuzou Nagata. Swirl Flow in Conical Diffusers. *The Japan Society of Mechanical Engineers*, 21(151), January 1978.

- 
- [9] Rafael Guarga F., Jesús Gracia S., Alejandro Sánchez H., and Eduardo Rodal C. LDV and Pressure Measurements in Swirling Confined, Turbulent and Non-cavitating Flows. 1985.
- [10] G. Mollenkopf and J. Raabe. Measurements of fluctuations of velocity and pressure in the draft tube of a francis turbine. 1970.
- [11] F.M. White. *Viscous Fluid Flow*. McGraw-Hill Series in Mechanical Engineering. McGraw-Hill Higher Education, 2006. ISBN 9780071244930.
- [12] Torbjørn Nielsen. Lecture notes in TEP4195: Turbomachinery, 2013.
- [13] Frank M White. *Fluid Mechanics*. McGraw Hill, 6 edition, 2008.
- [14] May 2014. URL <http://www.ltu.se/research/subjects/Stromningslara/Konferenser/Francis-99/Test-Case-1.111520>.
- [15] Joel Sundstrom, Kaveh Amiri, Carl Bergan, Michel Cervantes, and Ole Gunnar Dalhaug. LDA Measurements in the Francis-99 Draft Tube Cone. 2014.
- [16] May 2014. URL <http://sine.ni.com/ds/app/doc/p/id/ds-199/lang/no>.
- [17] June 2014. URL <http://mathworld.wolfram.com/Cross-Correlation.html>.
- [18] Z. Zhang, K. Eisele, and F. Hirt. The Influence of Phase-averaging Window Size on the Determination of Turbulence Quantities in Unsteady Turbulent Flows. *Experiments in Fluids*, 22(3):265–267, 1997.
- [19] H.C. Hulst and H.C. van de Hulst. *Light Scattering by Small Particles*. Dover Books on Physics Series. Dover Publications, 1957. ISBN 9780486642284.
- [20] Ruben Moritz. Transient CFD-Analysis of a High Head Francis Turbine. Master’s thesis, Norwegian University of Science and Technology, 2014.



# A | Laser Data Sheet

The data sheet for the laser system was obtained from the user manual of the LDA system. It describes in great detail the LDA system used in this thesis.

## SPECTRA-PHYSICS 177G HIGH POWER AIR-COOLED ION LASER SYSTEMS

PERFORMANCE SPECIFICATIONS<sup>1</sup>

Wavelength Specific Characteristics				
Wavelength	514	488	458	All Lines
Beam Diameter (mm)	0.82 ± 5%	0.82 ± 5%	0.82 ± 5%	0.82 ± 5%
Beam Divergence (mrad) (nominal)	0.78	0.78	0.78	0.78
Spatial Mode (TEM <sub>00</sub> )	M <sup>2</sup> < 1.2	M <sup>2</sup> < 1.2	M <sup>2</sup> < 1.2	M <sup>2</sup> < 1.2

Common Beam Characteristics	
Polarization Extinction Ratio	> 100:1 (E-vector vertical ± 5°)
Longitudinal Mode Spacing (nominal)	440 MHz
Beam Waist Location	Output of laser head

Stability <sup>2</sup>	
<b>Power</b>	
At turn on Stability over 2 hours <sup>3</sup>	> 95% of stabilized power ± 1%
<b>Beam Pointing</b>	
Angular	± 30 μrad/±3° C

Noise	
Switching Frequency Synchronous Periodic	≤ 3% peak to peak
<b>Broadband</b>	
10 Hz – 3 kHz	< 0.2% rms
10 Hz – 2 MHz	< 0.5% rms

- Specifications subject to change without notice.
- All measurements made in light control mode after a 30-minute warm-up, unless otherwise stated.
- Stability is measured over any 2-hour period after a 5-minute warm-up.
- Local control is provided by the 385F Remote Control when it is attached to the REMOTE INTERFACE connector on the 277G power supply. Remote operation is also possible when your equipment is attached to this connector (25-pin D-sub).

SERVICES AND OPERATING PARAMETERS<sup>1</sup>

Services and Equipment	
<b>Cooling Air Required</b>	
Laser Head	5.24 m <sup>3</sup> (185 CFM)
Power Supply	0.68 m <sup>3</sup> (24 CFM)
<b>Electric Service Required</b>	
Voltage (± 10%)	200 – 240 ac nominal
Current	16 A max
Frequency	47 – 63 Hz
Phase	Single
<b>Environmental</b>	
Temperature Range	4 – 40° C
Humidity (noncondensing)	0 – 95%
Altitude	0 – 3000 m (0 – 9800 ft)

Operating Parameters/Interfaces	
<b>Plasma Tube Operating Current Limits (nominal)</b>	
Minimum	4 A
Maximum	12 A
<b>Power Supply Switching Frequency</b>	
Nominal	100 kHz
<b>Power Supply Overall Efficiency</b>	
Nominal	> 90%
<b>Available Interface Provides These Controls<sup>4</sup></b>	
Power Adjust Power Monitor Interlock	Current Adjust Current Monitor Run/Standby

Compliance has been demonstrated to the following regulatory requirements for UL, CE and CDRH:

EN 50082-1: 1992	73/23/EEC: 1973
EN 55011: 1991	89/336/EEC: 1989
EN 60950: 1993	FCC Part 15 Class B
EN 61000-3-2: 1995	CDRH, 21 CFR 1040.10
EN 61010-1: 1993	UL 1950

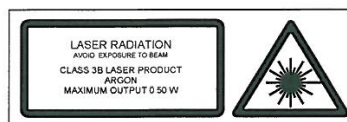


**Spectra-Physics**  
1335 Terra Bella Avenue  
Mountain View, CA 94043  
Tel: 1-800-775-2573  
Tel: 1-(650) 961-2550  
Fax: 1-(650) 964-3584  
e-mail: sales@splasers.com  
http://www.splasers.com

**Australia:** (61) 8-8443-8668  
**Belgium:** (31) 40 265 99 59  
**China:** (86) 10 6256 2934  
**France:** (33) 1 6918 63 11  
**Germany:** (49) 6151-708300  
**Hong Kong:** (852) 2523-5688  
**India:** (91) 80 6763 465

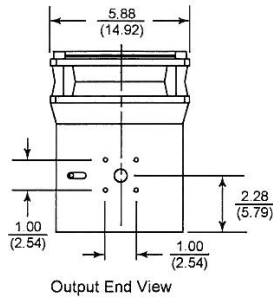
**Israel:** (972) 3-6356650  
**Italy:** (39) 02-57465-1  
**Japan: Tokyo** (81) 3-3794-5511  
**Osaka** (81) 6-6941-7331  
**Netherlands:** (31) 40 265 99 59  
**S. Korea:** (82) 2-587-8727  
**Spain:** (34) 91-3775006

**Scandinavia:** (46) 8-550 10403  
**Taiwan:** (886) 3-426-2376  
**UK:** (44) 1442-258100  
**Other European Countries:**  
(49) 6151-7080  
**Other Pacific Countries:**  
1-650-961-2550

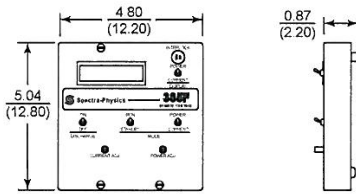


**SPECTRA-PHYSICS 177G HIGH POWER AIR-COOLED ION LASER SYSTEMS**

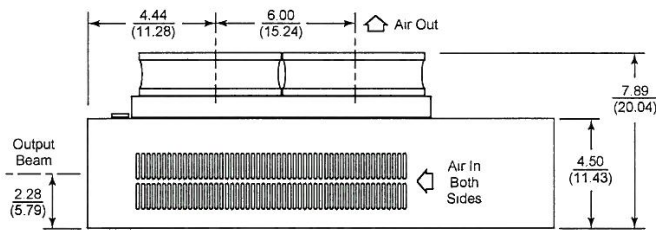
The Model 177G is the air-cooled ion laser of choice when maximum power is required. This laser delivers all of the advantages of the field-proven Model 163 lasers, including stability, reliability and easy plasma-tube replacement, while producing output powers of up to 500 mW. The plasma tube is based on Spectra-Physics' proven Metal/BeO tube technology and patented "Wavelength Selective Mirrors,"\* which ensures this laser will provide higher output power while maintaining exceptional lifetime. Power factor corrections to EN 61000-3-2: 1995, have been incorporated.



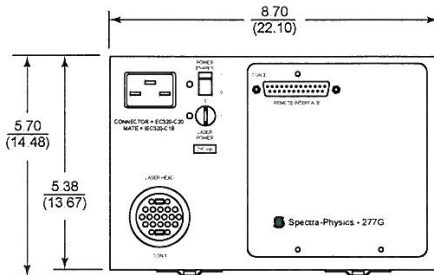
Output End View



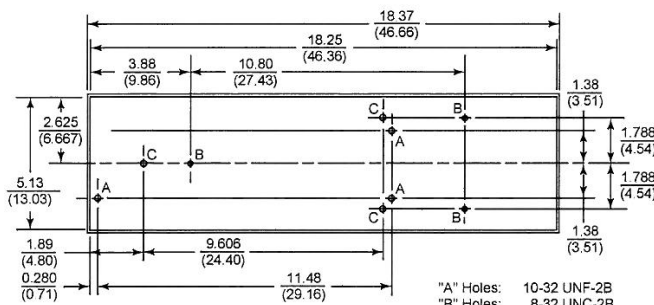
385F Remote Control



Side View

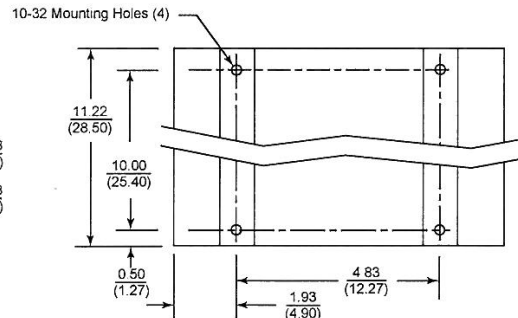


Control Panel



Bottom View  
177G Laser Head

"A" Holes: 10-32 UNF-2B  
 "B" Holes: 8-32 UNC-2B  
 "C" Holes: M5 Through



Bottom View  
277G Power Supply

\*Patent # 4,615,034

All dimensions in *inches*  
(*cm*)



Model 177G Laser Head	Model 277G Power Supply
<b>Size (L x W x H)</b>	
18.37 x 5.88 x 7.88 in. (46.66 x 14.94 x 20.02 cm)	11.22 x 8.70 x 5.70 in. (28.50 x 22.10 x 14.48 cm)
<b>Weight (actual/shipping)</b>	
22.0 lb (10.0 kg)/36.0 lb (16.3 kg)	15.0 lb (6.8 kg)/18.0 lb (8.2 kg)



## B | Calibration Documents

The calibration reports for the generator torque, the friction torque, flow rate, differential pressure, and inlet pressure can be found here. The calibrations were performed at the Waterpower Laboratory, following the standard procedures for this type of calibration.



# WATERPOWER LABORATORY

Date:

28.01.2014

Operator:

Carl Bergan  
Magni Svarstad

## Calibration Sheet

Calibration of flow meter

Calibrator: Weighing tank system

Unit: Flowmeter, reg nr. 4624-7 (A03 36133)

Calibration constants for weighing tank correction	a <sub>1</sub>	a <sub>2</sub>	a <sub>3</sub>	a <sub>4</sub>	a <sub>5</sub>
	3.73E-22	-8.71E-17	7.00E-12	-2.19E-07	1.00E+00

## Comments:

The flow rate changes during calibration. The inlet conditions to the pumps will change due to less water in the reservoir.

Corrected weight is calculated from for where parameters a,b,c,d and e is achil through substitution calibration.

$$W = a \cdot \frac{mW^5}{5} + b \cdot \frac{mW^4}{4} + c \cdot \frac{mW^3}{3} + d \cdot \frac{mW^2}{2} + e \cdot mW$$

Density of water is calculated from form  $\rho_w = (1 - 4,6699 \cdot 10^{-10} \cdot p_{abs}) + 8 \cdot 10^{-6} \cdot (\theta - 4 + 2,1318913 \cdot 10^{-7} \cdot p_{abs})^2 - 6 \cdot 10^{-8} \cdot (\theta - 4 + 2,1318913 \cdot 10^{-7} \cdot p_{abs})^3$

Density of air is calculated from formula  $\rho_a = \frac{(p_{abs} \cdot 3,4837 \cdot 10^3)}{(273,15 + \theta)}$

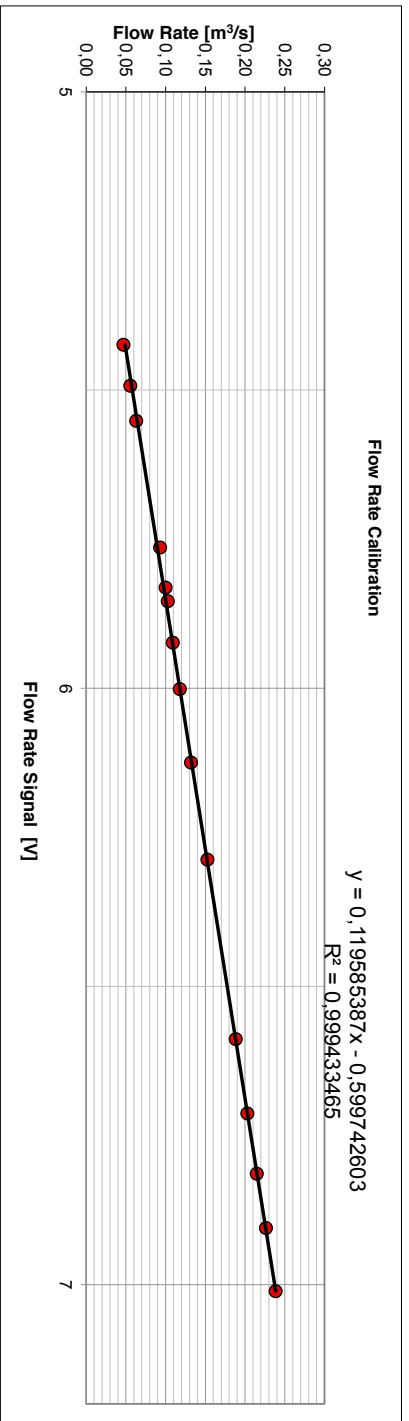
$$Q = \frac{W_2 - W_1}{\rho_w \cdot t \cdot (1 - \frac{\rho_a}{\rho_w})}$$

Discharge is found from formula

### Flow Rate Calibration

$$y = 0,119585387x - 0,599742603$$

$$R^2 = 0,999433465$$



Calibration constants, 28.01.2014	
C <sub>0</sub>	-0,59974
C <sub>1</sub>	0,11959

Date	Manual Observation before Weight [kg]	Manual Observation after Weight [kg]	Manual Observation Voltage [V]	Time [s]	Ambient pressure P <sub>amb</sub> [kPa]	Water temp T <sub>w</sub> [°C]	Air temp T <sub>a</sub> [°C]	Calculated value before Weight [kg]	Calculated value after Weight [kg]	Differential weight [kg]	Density of water [kg/m <sup>3</sup> ]	Density of air [kg/m <sup>3</sup> ]	Differential volume [m <sup>3</sup> ]	Calculated Flow Rate Q [m <sup>3</sup> /s]	Estimate Q [m <sup>3</sup> /s]	Deviation [%]
28.01.2014	22127.8	26789.8	5.424157	100.098	100.995	11.71	15.79	22127.9	26786.2	4658.3	999.5964	1.2185	4.66587	0.0466130	0.04891	4.69115
	26789.8	32329.8	5.492908	100.099	101.007	11.72	15.62	26786.2	32321.8	5535.6	999.5953	1.2194	5.54456	0.0553907	0.05713	3.04259
	32329.8	37353.4	5.551588	80.101	101.034	11.76	15.90	32321.8	37341.6	5019.9	999.5907	1.2185	5.02804	0.0627712	0.06415	2.14550
	37353.4	43963.0	5.764079	70.101	101.055	11.79	15.27	37341.6	43847.1	6505.4	999.5873	1.2215	6.51606	0.0929525	0.08956	-3.79140
	43863.0	49353.4	5.831367	55.102	101.052	11.72	15.19	43847.1	49334.6	5487.5	999.5953	1.2218	5.49643	0.0997502	0.09760	-2.19919
	49353.4	54479.4	5.854269	50.102	101.050	11.73	15.10	49334.6	54455.3	5123.7	999.5941	1.2221	5.13207	0.1024325	0.10034	-2.08298
	54479.4	58835.5	5.923835	40.101	101.044	11.73	15.04	54458.3	58812.7	4354.4	999.5941	1.2223	4.36149	0.1087626	0.10866	-0.09306
	58835.5	63553.4	6.001593	40.102	101.039	11.73	15.00	58812.7	63528.8	4716.2	999.5941	1.2224	4.72385	0.1177960	0.11796	0.13925
	63553.4	68831.6	6.124743	40.101	101.045	11.74	14.88	63528.8	68805.1	5276.3	999.5930	1.2230	5.28487	0.1317889	0.13269	0.67698
	42578.6	47922.5	6.287605	35.101	101.083	11.80	14.83	42563.4	47904.4	5340.9	999.5862	1.2237	5.34970	0.1524087	0.15216	-0.16144
	47922.5	53579.5	6.588682	30.102	101.086	11.80	14.80	47904.4	53555.8	5654.4	999.5862	1.2238	5.66366	0.1881491	0.18817	0.00977
	53579.5	59675.5	6.713098	30.101	101.101	11.79	14.79	53558.8	59652.3	6093.6	999.5873	1.2240	6.10359	0.2027703	0.20305	0.13571
	59675.5	66121.9	6.814321	30.101	101.096	11.83	14.76	59652.3	66096.4	6444.0	999.5828	1.2241	6.45463	0.2144325	0.21515	0.33378
	66121.9	61798.4	6.905254	30.101	101.092	11.83	14.74	61798.4	61774.5	6794.6	999.5828	1.2242	6.80578	0.2260980	0.22602	-0.03235
	61798.4	68956.8	7.011138	30.101	101.097	11.87	14.70	61774.5	68930.2	7155.8	999.5782	1.2244	7.16756	0.2381171	0.23869	0.23877

# CALIBRATION REPORT

---

**CALIBRATION PROPERTIES**

Calibrated by: Carl Bergan  
Type/Producer: FHCW36W1-ACKAY / Fuji Electric  
SN: N3M7766T  
Range: -50 - 50 bar  
Unit: kPa

**CALIBRATION SOURCE PROPERTIES**

Type/Producer: Pressurements deadweight tester P3223-1  
SN: 66256  
Uncertainty [%]: 0,01

**POLY FIT EQUATION:**

$Y = -123.4925116E+3X^0 + 62.6940117E+3X^1$

**CALIBRATION SUMMARY:**

Max Uncertainty : Inf [%]  
Max Uncertainty : 0.11945150 [kPa]  
RSQ : 1.000000  
Calibration points : 31

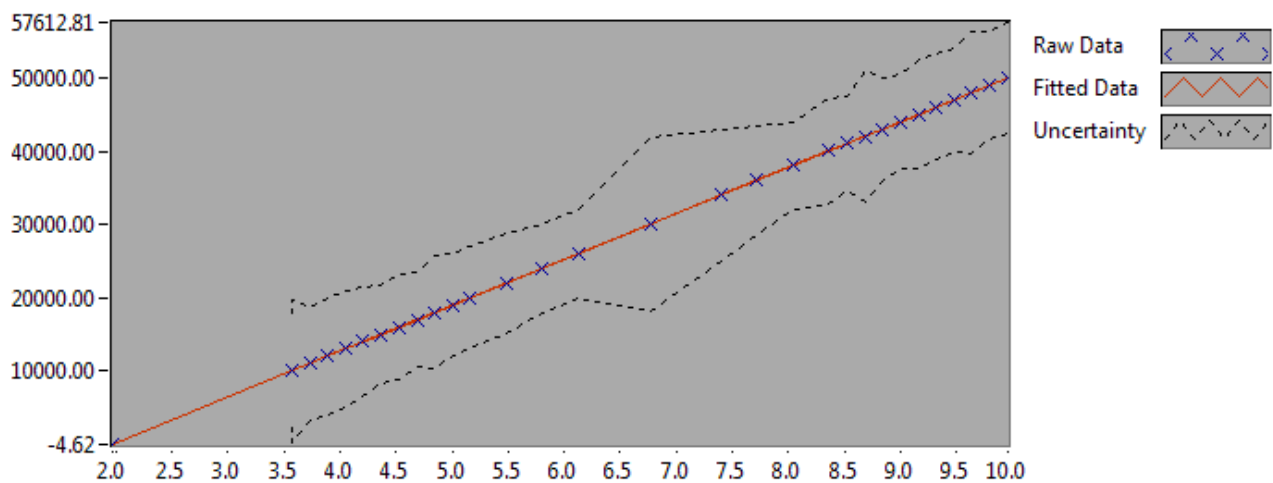


Figure 1 : Calibration chart (The uncertainty band is multiplied by 1000 )

---

Carl Bergan

---



**CALIBRATION VALUES**

Value [kPa]	Voltage [V]	Best Poly Fit [kPa]	Deviation [kPa]	Uncertainty [%]	Uncertainty [kPa]
100.15107096	3.568514	100.23194381	-0.08087286	0.078017	0.07813460
110.16617805	3.728806	110.28131534	-0.11513728	0.069667	0.07674990
120.18128515	3.887419	120.22538384	-0.04409870	0.065701	0.07896064
130.19639224	4.047206	130.24307170	-0.04667946	0.061127	0.07958517
140.21149934	4.205739	140.18214229	0.02935705	0.053951	0.07564578
150.22660644	4.366537	150.26323251	-0.03662607	0.044391	0.06668730
160.24171353	4.525215	160.21139279	0.03032074	0.044800	0.07178866
170.25682063	4.684813	170.21719787	0.03962276	0.038009	0.06471346
180.27192772	4.846488	180.35327244	-0.08134472	0.042415	0.07646212
190.28703482	5.004530	190.26156363	0.02547118	0.036347	0.06916286
200.30214191	5.162530	200.16722868	0.13491323	0.034843	0.06979034
220.33235611	5.481835	220.18572320	0.14663291	0.030977	0.06825306
240.36257030	5.801508	240.22732202	0.13524828	0.025258	0.06070966
260.39278449	6.121151	260.26701631	0.12576818	0.023296	0.06066156
300.45321287	6.764796	300.61967074	-0.16645787	0.039757	0.11945150
340.51364125	7.399644	340.42084282	0.09279843	0.026285	0.08950298
360.54385545	7.721100	360.57421222	-0.03035677	0.020555	0.07411008
380.57406964	8.037890	380.43508505	0.13898458	0.015876	0.06041961
400.60428383	8.360698	400.67320123	-0.06891740	0.018127	0.07261675
410.61939092	8.518145	410.54415357	0.07523735	0.015897	0.06527732
420.63449802	8.681732	420.80006677	-0.16556876	0.021281	0.08951393
430.64960511	8.838419	430.62340630	0.02619882	0.016469	0.07092244
440.66471221	8.998681	440.67090756	-0.00619535	0.014683	0.06470099
450.67981931	9.158291	450.67751380	0.00230551	0.016641	0.07499894
460.69492640	9.317464	460.65669249	0.03823391	0.015766	0.07263225
470.71003350	9.477423	470.68515556	0.02487793	0.014922	0.07023966
480.72514059	9.636606	480.66498479	0.06015581	0.017254	0.08294249
490.74024769	9.798846	490.83644408	-0.09619639	0.014973	0.07347674
500.75535478	9.958927	500.87256862	-0.11721383	0.015028	0.07525550
100.15107096	3.569086	100.26777774	-0.11670679	0.096805	0.09695141
0.000000	1.969028	-0.04624555	0.04624555	Inf	NaN

**COMMENTS:**

The uncertainty is calculated with 95% confidence. The uncertainty includes the randomness in the calibrated instrument during the calibration, systematic uncertainty in the instrument or property which the instrument under calibration is compared with (dead weight manometer, calibrated weights etc.), and due to regression analysis to fit the calibration points to a linear calibration equation. The calculated uncertainty can be used as the total systematic uncertainty of the calibrated instrument with the given calibration equation.

# CALIBRATION REPORT

## CALIBRATION PROPERTIES

Calibrated by: Carl Bergan  
Type/Producer: FHCW36W1-ACKAY / Fuji Electric  
SN: N3M7762T  
Range: -50 - 50 bar  
Unit: kPa

## CALIBRATION SOURCE PROPERTIES

Type/Producer: Pressurements deadweight tester P3223-1  
SN: 66256  
Uncertainty [%]: 0,01

## POLY FIT EQUATION:

$Y = -123.4029305E+3X^0 + 62.6675364E+3X^1$

## CALIBRATION SUMMARY:

Max Uncertainty : Inf [%]  
Max Uncertainty : 0.08238731 [kPa]  
RSQ : 1.000000  
Calibration points : 30

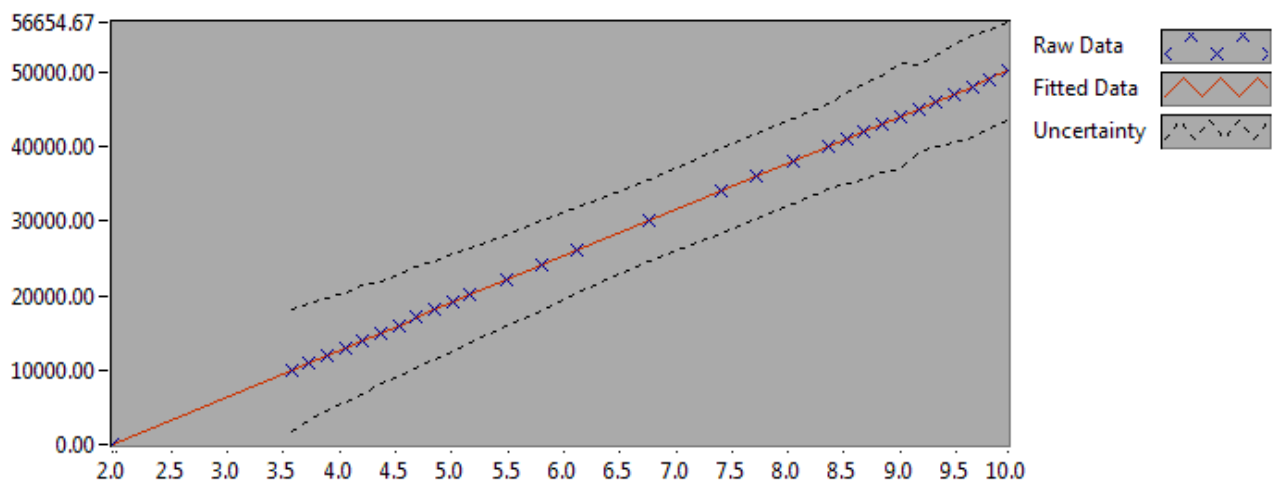


Figure 1 : Calibration chart (The uncertainty band is multiplied by 1000 )

---

Carl Bergan

---

**CALIBRATION VALUES**

Value [kPa]	Voltage [V]	Best Poly Fit [kPa]	Deviation [kPa]	Uncertainty [%]	Uncertainty [kPa]
0.000000	1.975083	0.37065083	-0.37065083	Inf	NaN
100.15107096	3.567598	100.16962074	-0.01854979	0.082263	0.08238731
110.16617805	3.727182	110.17040291	-0.00422486	0.070363	0.07751579
120.18128515	3.886257	120.13919505	0.04209010	0.062481	0.07509030
130.19639224	4.046721	130.19510559	0.00128665	0.056863	0.07403338
140.21149934	4.206555	140.21148661	0.00001273	0.052981	0.07428499
150.22660644	4.366058	150.20719170	0.01941474	0.045691	0.06864049
160.24171353	4.525651	160.20846578	0.03324775	0.043076	0.06902508
170.25682063	4.685033	170.19656377	0.06025686	0.040731	0.06934736
180.27192772	4.845520	180.25386611	0.01806161	0.036399	0.06561766
190.28703482	5.004610	190.22364069	0.06339413	0.034469	0.06558975
200.30214191	5.164502	200.24369873	0.05844319	0.031441	0.06297703
220.33235611	5.483303	220.22213608	0.11022002	0.027966	0.06161770
240.36257030	5.803237	240.27164610	0.09092420	0.025286	0.06077768
260.39278449	6.123783	260.35943944	0.03334505	0.021861	0.05692380
300.45321287	6.762144	300.36398327	0.08922960	0.018367	0.05518412
340.51364125	7.402044	340.46492528	0.04871597	0.016989	0.05785083
360.54385545	7.721382	360.47705527	0.06680018	0.016125	0.05813864
380.57406964	8.041240	380.52176449	0.05230514	0.015111	0.05750792
400.60428383	8.361462	400.58928744	0.01499639	0.014245	0.05706766
410.61939092	8.521777	410.63581110	-0.01642018	0.014788	0.06072124
420.63449802	8.681091	420.61963846	0.01485956	0.015406	0.06480335
430.64960511	8.841386	430.66493558	-0.01533047	0.014914	0.06422514
440.66471221	9.000692	440.64825390	0.01645831	0.015969	0.07036982
450.67981931	9.161257	450.71049160	-0.03067230	0.013138	0.05921241
460.69492640	9.321747	460.76797292	-0.07304652	0.013339	0.06145330
470.71003350	9.480984	470.74696393	-0.03693044	0.013958	0.06570405
480.72514059	9.641579	480.81105685	-0.08591626	0.014141	0.06797985
490.74024769	9.801412	490.82744223	-0.08719454	0.013352	0.06552514
500.75535478	9.961352	500.85048081	-0.09512602	0.013119	0.06569623

**COMMENTS:**

The uncertainty is calculated with 95% confidence. The uncertainty includes the randomness in the calibrated instrument during the calibration, systematic uncertainty in the instrument or property which the instrument under calibration is compared with (dead weight manometer, calibrated weights etc.), and due to regression analysis to fit the calibration points to a linear calibration equation. The calculated uncertainty can be used as the total systematic uncertainty of the calibrated instrument with the given calibration equation.

# CALIBRATION REPORT

---

## CALIBRATION PROPERTIES

Calibrated by: Carl Bergan

Type/Producer:

SN: V4331-9

Range:

Unit: kg

## CALIBRATION SOURCE PROPERTIES

Type/Producer: Calibrated weights from the Norwegian Metrology Service

SN: -

Uncertainty [%]: -

## POLY FIT EQUATION:

$Y = + 4.94233453E+0X^0 + 3.56050316E+0X^1$

## CALIBRATION SUMMARY:

Max Uncertainty : 3.050197 [%]

Max Uncertainty : 0.195622 [Nm]

RSQ : 0.996974

Calibration points : 20

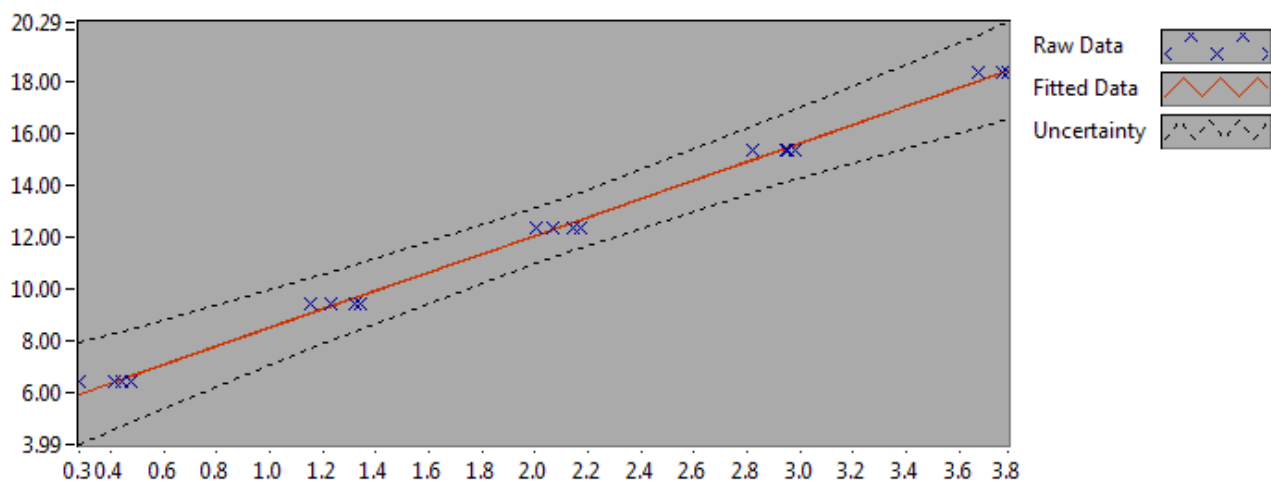


Figure 1 : Calibration chart (The uncertainty band is multiplied by 10 )

---

Carl Bergan

---

**CALIBRATION VALUES**

Value [Nm]	Voltage [V]	Best Poly Fit [Nm]	Deviation [Nm]	Uncertainty [%]	Uncertainty [Nm]
6.413417	0.282346	5.947627	0.465790	3.050197	0.195622
9.392601	1.156561	9.060273	0.332328	1.451454	0.136329
12.371785	2.004324	12.078738	0.293048	0.868079	0.107397
15.350969	2.823888	14.996796	0.354174	0.822492	0.126261
18.330154	3.671944	18.016302	0.313852	0.977586	0.179193
18.330154	3.759031	18.326378	0.003776	1.012307	0.185557
15.350969	2.950999	15.449377	-0.098408	0.864223	0.132667
12.371785	2.143939	12.575837	-0.204052	0.866651	0.107220
9.392601	1.319573	9.640678	-0.248077	1.359450	0.127688
6.413417	0.444982	6.526693	-0.113276	2.859470	0.183390
6.413417	0.414234	6.417216	-0.003800	2.894625	0.185644
9.392601	1.233979	9.335922	0.056679	1.406125	0.132072
12.371785	2.065743	12.297419	0.074366	0.865852	0.107121
15.350969	2.945771	15.430761	-0.079791	0.862500	0.132402
18.330154	3.762655	18.339281	-0.009128	1.013819	0.185835
18.330154	3.783015	18.411773	-0.081619	1.022025	0.187339
15.350969	2.980893	15.555812	-0.204843	0.874880	0.134302
12.371785	2.170794	12.671452	-0.299667	0.867867	0.107371
9.392601	1.342211	9.721281	-0.328680	1.347812	0.126595
6.413417	0.475706	6.636088	-0.222671	2.824769	0.181164

**COMMENTS:**


---

The uncertainty is calculated with 95% confidence. The uncertainty includes the randomness in the calibrated instrument during the calibration, systematic uncertainty in the instrument or property which the instrument under calibration is compared with (dead weight manometer, calibrated weights etc.), and due to regression analysis to fit the calibration points to a linear calibration equation. The calculated uncertainty can be used as the total systematic uncertainty of the calibrated instrument with the given calibration equation.

# CALIBRATION REPORT

---

**CALIBRATION PROPERTIES**

Calibrated by: Carl Bergan  
Type/Producer: HBM Z6FC3  
SN: V4536-4  
Range: 50-500 kg  
Unit: kg

**CALIBRATION SOURCE PROPERTIES**

Type/Producer: Calibrated weights from the Norwegian Metrology Service  
SN:  
Uncertainty [%]:

**POLY FIT EQUATION:**

$Y = -194.76444248E+0X^0 + 483.04451254E+0X^1$

**CALIBRATION SUMMARY:**

Max Uncertainty : Inf [%]  
Max Uncertainty : 8.452808 [Nm]  
RSQ : 0.999220  
Calibration points : 62

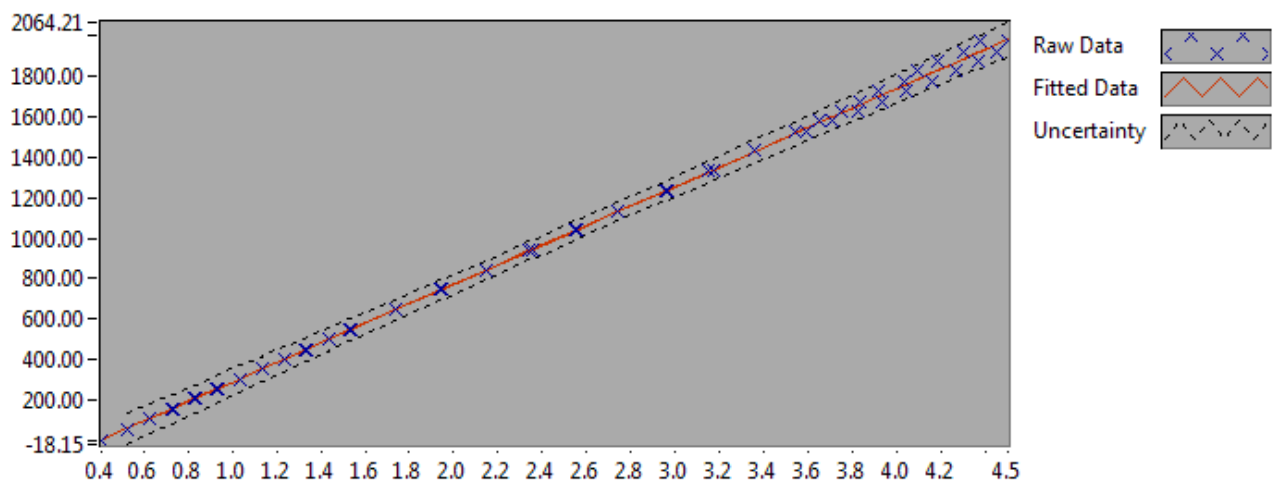


Figure 1 : Calibration chart (The uncertainty band is multiplied by 10 )

---

Carl Bergan

---

**CALIBRATION VALUES**

<b>Value [kPa]</b>	<b>Voltage [V]</b>	<b>Best Poly Fit [kPa]</b>	<b>Deviation [kPa]</b>	<b>Uncertainty [%]</b>	<b>Uncertainty [kPa]</b>
0.000000	0.410646	3.595961	-3.595961	Inf	NaN
58.977897	0.529835	61.169460	-2.191563	13.407204	7.907287
107.986952	0.630283	109.690456	-1.703504	7.065710	7.630045
156.996987	0.731147	158.412290	-1.415303	4.686240	7.357256
206.005258	0.831619	206.944393	-0.939135	3.442486	7.091701
255.009020	0.931386	255.136282	-0.127262	2.680214	6.834787
304.021113	1.035067	305.219148	-1.198036	2.163003	6.575986
353.033010	1.132356	352.213670	0.819340	1.796264	6.341404
402.048337	1.234668	401.635295	0.413043	1.518360	6.104540
451.058372	1.330344	447.850784	3.207589	1.306529	5.893210
500.073406	1.438344	500.019922	0.053484	1.133380	5.667731
549.086381	1.540121	549.182498	-0.096117	0.996124	5.469582
647.103020	1.741200	646.312688	0.790332	0.791997	5.125040
745.123188	1.947096	745.769782	-0.646594	0.650646	4.848113
843.139827	2.147145	842.402091	0.737737	0.553365	4.665645
941.118242	2.351661	941.192738	-0.074495	0.486476	4.578313
1039.116945	2.549372	1036.695846	2.421099	0.442080	4.593730
1137.101731	2.743416	1130.427749	6.673981	0.413694	4.704121
1235.089555	2.957853	1234.010046	1.079508	0.399043	4.928538
1333.069734	3.145622	1324.710785	8.358948	0.390189	5.201493
1431.046384	3.360490	1428.501789	2.544595	0.390509	5.588360
1529.024113	3.537953	1514.224575	14.799538	0.389636	5.957631
1578.014741	3.648419	1567.584175	10.430566	0.393305	6.206415
1627.003606	3.746582	1615.001447	12.002159	0.395663	6.437445
1676.002075	3.831716	1656.124927	19.877148	0.396516	6.645617
1724.989959	3.917986	1697.797167	27.192792	0.397820	6.862360
1773.978824	4.034160	1753.914646	20.064177	0.403788	7.163105
1822.975039	4.094789	1783.200834	39.774205	0.401768	7.324121
1871.970372	4.186937	1827.712680	44.257691	0.404472	7.571590
1920.963255	4.302142	1883.361417	37.601838	0.410692	7.889244
1969.964566	4.372498	1917.346524	52.618042	0.410464	8.085992
1969.964566	4.501549	1979.683916	-9.719350	0.429084	8.452808
1920.963255	4.454698	1957.052856	-36.089602	0.433041	8.318562
1871.970372	4.369423	1915.861315	-43.890944	0.431475	8.077078
1822.975039	4.268232	1866.981609	-44.006571	0.427579	7.794661
1773.978824	4.160712	1815.044851	-41.066028	0.422810	7.500555
1724.989959	4.041867	1757.637047	-32.647088	0.416415	7.183124
1676.002075	3.935476	1706.245864	-30.243789	0.412111	6.906994
1627.003606	3.826877	1653.787511	-26.783906	0.407718	6.633594
1578.014741	3.710861	1597.746685	-19.731943	0.402565	6.352529
1529.024113	3.594883	1541.724191	-12.700078	0.397910	6.084138
1431.046384	3.360998	1428.747314	2.299070	0.390595	5.589589
1333.069734	3.172108	1337.504695	-4.434962	0.393563	5.246471





## C | Phase-resolved results

Phase-resolved velocity is available here for all operating points at both measuring sections.

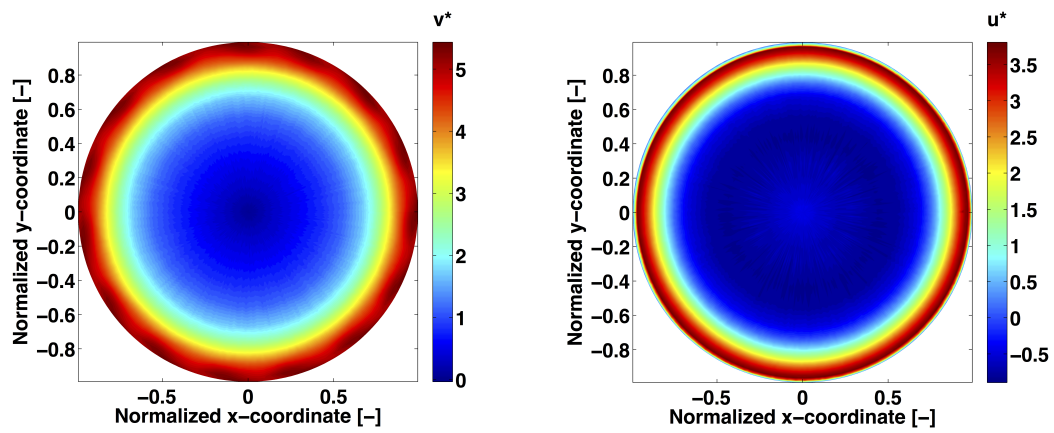


FIGURE C.1: Phase resolved tangential (left) and axial (right) velocity for part load, position I.

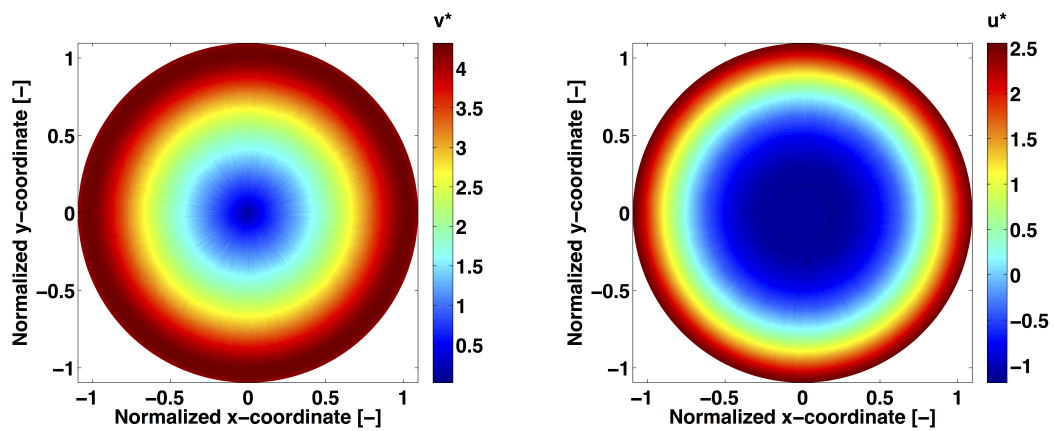


FIGURE C.2: Phase resolved tangential (left) and axial (right) velocity for part load, position II.

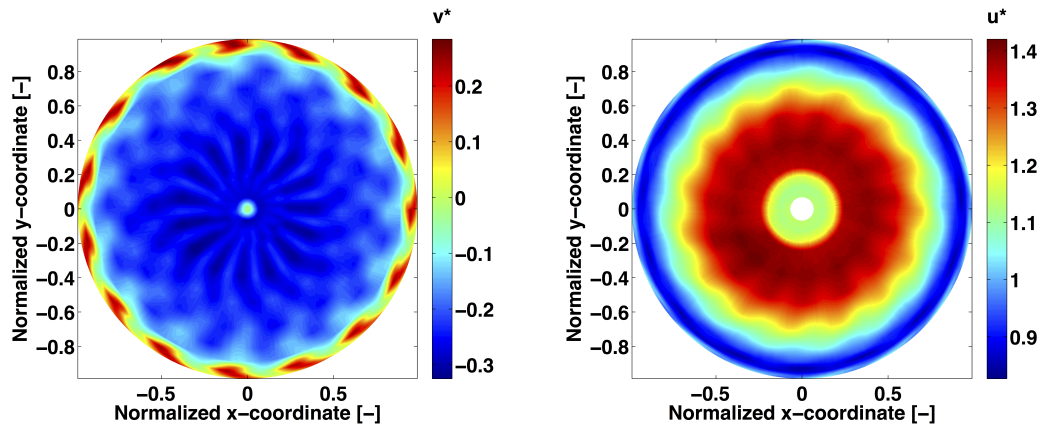


FIGURE C.3: Phase resolved tangential (left) and axial (right) velocity for BEP, position I.

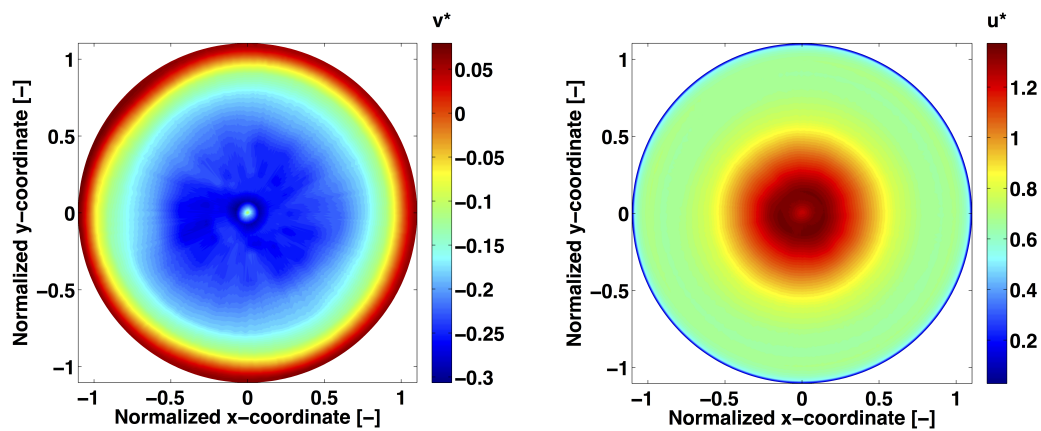


FIGURE C.4: Phase resolved tangential (left) and axial (right) velocity for BEP, position II.

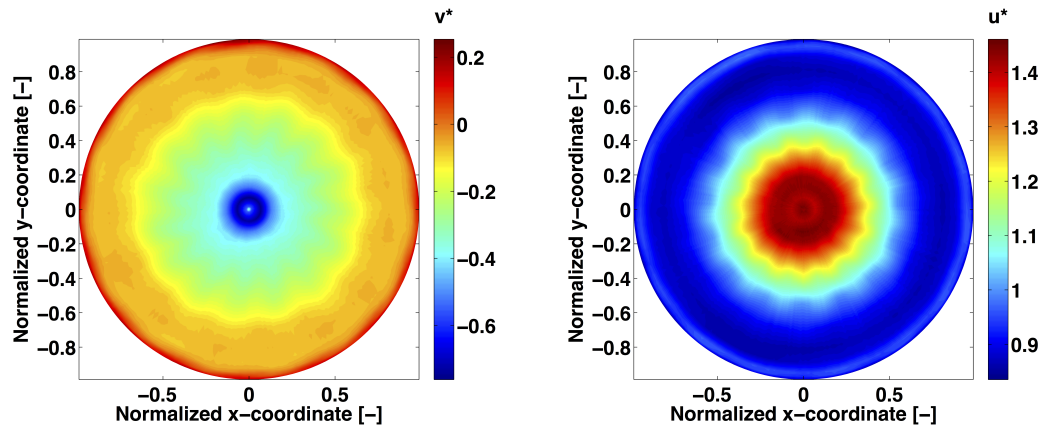


FIGURE C.5: Phase resolved tangential (left) and axial (right) velocity for full load, position I.

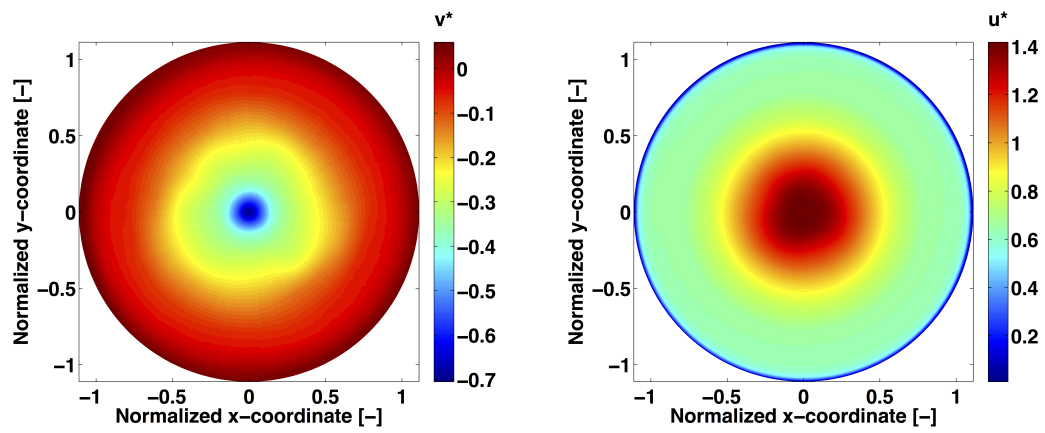


FIGURE C.6: Phase resolved tangential (left) and axial (right) velocity for full load, position II.